THE ASTROPHYSICAL JOURNAL, 562:824–841, 2001 December 1


# MOLECULAR LINE EMISSIONS FROM THE PHOTODISSOCIATION REGION OF NGC 7027

TATSUHIKO I. HASEGAWA AND SUN KWOK[1]
Department of Physics and Astronomy, University of Calgary, AB T2N 1N4, Canada; hasegawa@iras.ucalgary.ca, kwok@iras.ucalgary.ca
*Received 2001 April 7; accepted 2001 August 6*

## ABSTRACT

We have observed or searched for 11 molecular species in 17 transitions in the 200 and 300 GHz bands in the young planetary nebula NGC 7027. The results include a first detection of $C_2H$ in this source. The observed spectra of $HCO^+$, $H^{13}CO^+$, HCN, CN, $C_2H$, and $CO^+$ show line widths wider than that of bulk CO emission but coincident with the full width at detection limit of weak wings in CO spectra. The $HCO^+$, HCN, and CN emitting regions have a size of about 13″, significantly smaller than that of the CO emitting region. Thus, the emission of all the observed molecules other than CO and $^{13}CO$ must originate from a very small volume compared with the entire CO envelope. Excitation analyses of six molecules with electron and neutral collisions at a gas temperature of 800 K yield similar density estimates ranging from 1.3 to $5 \times 10^5$ cm$^{-3}$. Estimated column densities for $HCO^+$, HCN, CN, $CO^+$, and $C_2H$ are in good agreement with predictions by a chemical model for the photodissociation region of NGC 7027. These analyses suggest that photochemistry is active in NGC 7027 and the observed molecular emissions (except CO) originate from the $H_2$ photodissociation zone of the object.

*Subject headings:* ISM: molecules — planetary nebulae: individual (NGC 7027) — radio lines: ISM

## 1. INTRODUCTION

NGC 7027 is a young planetary nebula with a hot central star ($T_* \sim 200{,}000$ K; Latter et al. 2000). It has an extremely rich emission-line spectrum (with over 1000 lines identified; Péquignot 1997) and is one of the most extensively studied objects in the sky. Its 10″ ionized shell is surrounded by an extended molecular envelope of size greater than 70″ (Bieging, Wilner, & Thronson 1991). A thin shell of molecular hydrogen emission separates the ionized shell and the molecular envelope (Graham et al. 1993). Recent *Infrared Space Observatory* (*ISO*) observations of the high rotational lines of CO suggest that these lines originate from a small, warm, dense region (Volk & Kwok 1997; Justtanont et al. 2000). The combination of a strong UV source and a molecular envelope makes NGC 7027 a unique laboratory for the study of chemistry in a photon-dominated region (PDR) (Yan et al. 1999; Hasegawa, Volk, & Kwok 2000).

In comparison to interstellar molecular clouds, circumstellar envelopes (CSEs) offer many advantages for the understanding of the chemical process responsible for the formation of molecular species. First, there is only one heating source (the central star), the properties of which can be reasonably well determined by other techniques. The geometry of the envelope is simple, almost in all cases having a certain degree of symmetry. Since the molecular envelope undergoes systematic expansion, the timescale of the chemical processes is well constrained by the dynamical age of the envelope. Most of the molecular line profiles have well-defined shapes that give valuable clues to the kinematics of the envelope. Similarity in profile shapes from different lines also provides evidence that they arise from the same emitting region under similar physical conditions. This affords us a much higher degree of confidence in the derivation of the relative molecular abundances. In the case of NGC 7027, high-resolution images are available in the radio (from *f-f* continuum; Masson 1986), millimeter (from CO and $HCO^+$; Graham et al. 1993; Deguchi et al. 1992; Likkel 1992; Bieging et al. 1991), mid-infrared (from dust emission; Dayal et al. 1999; Arens et al. 1984; Aitken & Roche 1983), near-infrared (from nebular emission and $H_2$; Latter et al. 2000; Hora, Latter, & Deutsch 1999; Cox et al. 1997; Kastner et al. 1996; Graham et al. 1993), optical (from recombination and forbidden lines; Robberto et al. 1993), and X-ray (from hot ionized gas; Kastner, Vrtilek, & Soker 2001). These complementary data give us a good understanding of the physical environment and impose a high degree of constraints on any chemical and physical models.

For the first time, the observations of molecular ions as well as other products of photochemistry provide us with the data necessary for a detailed study of PDR chemistry. In this paper we report on the observations of 11 molecular species in NGC 7027. From the observed line strengths and distributions, the abundances of these species are derived and compared with chemical models.

## 2. OBSERVATIONS

The observations were obtained with the James Clarke Maxwell Telescope (JCMT) in 1998 September and in 1999 June–October. Additional observations were obtained in 2000 July. Common user receivers RxB3 and RxA3i were used for the 300 and 200 GHz band observations, respectively. RxB3 is a single-sideband, dual-polarization channel receiver with a typical system temperature of about 500 K. RxA3i is a double-sideband, single-polarization channel receiver with a typical system temperature of about 400 K. The 200 GHz data were originally obtained at a frequency resolution of 189 kHz with an instantaneous bandwidth of 250 MHz. The 300 GHz data were obtained at a frequency resolution of 756 kHz with an instantaneous bandwidth of 500 MHz. The data were later processed (several channels were binned, and the frequency resolution was reduced) to reduce the noise level. The observation was carried out in a beam switching mode with an azimuth beam throw of 2′. Seasonal and day-to-day variations of intensity scale were about 10%, which we adopt as the calibration uncertainty

[1] Canada Council Killam Fellow.

in this paper. The observations were originally represented as the antenna temperature $T_A^*$, which had been corrected for antenna losses and atmospheric attenuation. The antenna temperature was converted to the main beam temperature $T_{MB}$ with $T_{MB} = T_A^*/\eta_B$, where $\eta_B$ is the main beam efficiency. In this paper, most of the intensities will be expressed as $T_{MB}$. During the 1998–2000 period, the JCMT had $\eta_B = 0.63$ (300 GHz band) and $\eta_B = 0.69$ (200 GHz band). Also during the same period, the JCMT had beam sizes (full width at half-power) of 13.″2 (300 GHz band) and 19.″7 (200 GHz band). Pointing was checked every 60–90 minutes. The pointing uncertainty is about 2″ in azimuth and elevation. The adopted position for NGC 7027 was $\alpha(1950) = 21^h05^m09^s.4$ and $\delta(1950) = 42°02'03''$.

### 2.1. *Results*

A total of 11 species (17 rotational transitions) were observed or searched for. The observed molecules and transitions are given in Table 1. Standard spectra of CO (2–1) and $^{13}CO$ (2–1) were obtained in 1999 October. Other observatory standard spectra of CO (3–2, 4–3) and $^{13}CO$ (3–2) were obtained from the JCMT archive. Most of the lines were measured at the central position only. Small maps were made in $HCO^+$ (4–3, 3–2), HCN (4–3), and CN (3–2) at sampling intervals of 5″, 10″, 7″, and 10″, respectively. Five-point observations were made in $H^{13}CO^+$ (4–3), $C_2H$ (4–3), and $HCS^+$ (8–7) at a sampling interval of 5″. The spectra at the central position are presented in Figures 1 (300 GHz lines), 2 (200 GHz lines), and 3 (weak lines and negative results). Table 1 gives a summary of line parameters for the spectra in Figures 1–3. Also included in Table 1 are assumed frequencies, integrated main beam temperatures at the central position, rms noise levels $\sigma_{MB}$ (in $T_{MB}$ scale) at a reduced frequency resolution $\Delta v$, peak $T_{MB}$ (the highest value in a profile), radial velocities of the peak $T_{MB}$ in $V_{LSR}$, and sampling information.

$C_2H$ has been detected for the first time in NGC 7027 in this study. The $C_2H$ $N = 3$–2, $J = 7/2$–5/2, and $J = 5/2$–3/2 hyperfine groups are clearly seen in Figure 2, and the $C_2H$ $N = 4$–3, $J = 9/2$–7/2, and $J = 7/2$–5/2 hyperfine groups are seen in Figure 1. $H^{13}CO^+$ (Apponi, Pesch, & Ziurys 1999) has been confirmed in this study. The $J = 4$–3 and 3–2 lines of $H^{13}CO^+$ are clearly seen in Figures 1 and 2.

Our observations of $CO^+$ $N = 3$–2, $J = 7/2$–5/2 (Fig. 1) and $N = 2$–1, $J = 3/2$–1/2 (Fig. 3) confirm the presence of this molecular ion in NGC 7027. In the first detection of $CO^+$ by Latter, Walker, & Maloney (1993), only $CO^+$ $N = 2$–1, $J = 5/2$–3/2 was observed. We have observed $CO^+$ $N = 3$–2, $J = 7/2$–5/2, and $J = 5/2$–3/2 simultaneously. The entire spectrum is shown in Figure 4, where the rest frequency has been adjusted for $J = 7/2$–5/2. Unfortunately, the $J = 5/2$–3/2 component is blended with He26α and close to H26α both originating from the ionized region. We made Gaussian model profiles of H26α and He26α based on the observation in Figure 4 and on past observations of H and He recombination lines in the radio band (Vallèe et al. 1990). A common line width of 43 km $s^{-1}$ is assumed for the H and He lines, and an intensity ratio He/H of 0.136 is assumed (Vallèe et al. 1990). Then, the observed partial profile of H26α in Figure 4 was fitted with a Gaussian profile, and the He26α profile was estimated from the best-fit H26α parameters. Carbon recombination lines have

TABLE 1

SUMMARY OF OBSERVATIONS

| Molecular Species | Transition (upper → lower) | Frequency (GHz) | $\int T_{MB}\,dV$ (K km $s^{-1}$) | $T_{MB}$ (K) | $V_{LSR}$ (km $s^{-1}$) | $\sigma_{MB}/\Delta v$ (K $MHz^{-1}$) | Sampling Pattern |
|---|---|---|---|---|---|---|---|
| $HCO^+$ ..... | $J = 4$–3 | 356.7342 | 68.67±0.30 | 2.34 | 33.6 | 0.041/1.25 | 70″ × 20″ map at 5″ |
| | $J = 3$–2 | 267.5576 | 55.41±0.22 | 2.07 | 34.2 | 0.052/1.25 | 40″ × 40″ map at 10″ |
| $H^{13}CO^+$ ..... | $J = 4$–3 | 346.9977 | 1.30±0.15 | 0.043 | 26.7 | 0.014/2.50 | Five-point at 5″ |
| | $J = 3$–2 | 260.2555 | 1.45±0.11 | 0.043 | 25.9 | 0.013/1.25 | One-point |
| $CO^+$ ..... | $N = 3$–2: | | | | | | |
| | $J = 7/2$–5/2 | 354.0142 | 1.24±0.17 | 0.032 | 21.4 | 0.014/2.50 | One-point |
| | $J = 5/2$–3/2 | 353.7412 | See text | | | 0.014/2.50 | One-point |
| | $N = 2$–1: | | | | | | |
| | $J = 3/2$–1/2 | 235.7896 | 0.87±0.13 | 0.020 | 26.5 | 0.009/2.50 | One-point |
| HCN ..... | $J = 4$–3 | 354.5055 | 22.52±0.35 | 1.05 | 40.1 | 0.048/1.25 | 40″ × 40″ map at 10″ |
| | $J = 3$–2 | 265.8864 | 20.44±0.75 | 0.82 | 39.5 | 0.090/1.25 | One-point |
| CN ..... | $N = 3$–2: | | | | | | |
| | $J = 7/2$–5/2 | 340.2479 | 35.49±0.67 | 1.30 | 40.5 | 0.07/1.25 | 50″ × 50″ map at 7″ |
| | $J = 5/2$–3/2 | 340.0316 | 27.79±0.61 | 1.11 | 37.0 | 0.07/1.25 | 50″ × 50″ map at 7″ |
| $C_2H$ ..... | $N = 4$–3: | | | | | | |
| | $J = 9/2$–7/2 | 349.3381 | 6.98±0.24 | 0.319 | 40.8 | 0.032/1.25 | Five-point at 5″ |
| | $J = 7/2$–5/2 | 349.4006 | 5.94±0.25 | 0.235 | 41.1 | 0.032/1.25 | Five-point at 5″ |
| | $N = 3$–2: | | | | | | |
| | $J = 7/2$–5/2 | 262.0045 | 4.14±0.13 | 0.128 | 40.0 | 0.013/1.25 | One-point |
| | $J = 5/2$–3/2 | 262.0652 | 2.81±0.13 | 0.103 | 39.0 | 0.013/1.25 | One-point |
| $HCS^+$ ..... | $J = 6$–5 | 256.0278 | 0.40±0.10 | 0.025 | 19.0 | 0.006/10.0 | One-point |
| | $J = 8$–7 | 341.3508 | ...±0.083 | ... | ... | 0.008/1.25 | Five-point at 5″ |
| $H_3O^+$ ..... | $J_K = 3_2^+ - 2_2^+$ | 364.7974 | ...±0.24 | ... | ... | 0.024/2.50 | One-point |
| $HCNH^+$ ..... | $J = 3$–2 | 222.3294 | ...±0.11 | ... | ... | 0.012/1.25 | One-point |
| CS ..... | $J = 5$–4 | 244.9356 | ...±0.14 | ... | ... | 0.016/1.25 | One-point |
| $SO^+$ ..... | $J = 11/2$–9/2($f$) | 255.3532 | ...±0.22 | ... | ... | 0.026/1.25 | One-point |
| CO ..... | $J = 2$–1 | 230.5380 | 341.49±0.58 | 13.46 | 27.3 | 0.09/0.625 | One-point |
| $^{13}CO$ ..... | $J = 2$–1 | 220.3980 | 14.42±0.71 | 0.66 | 13.4 | 0.077/1.25 | One-point |

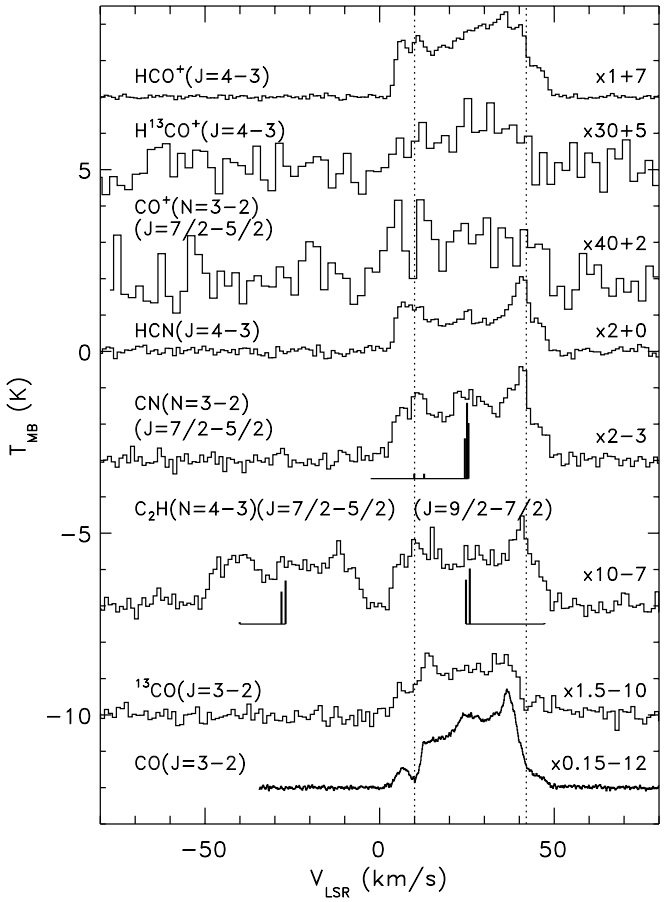


FIG. 1.—300 GHz band spectra at the central position of NGC 7027. Molecules and transitions are indicated in the figure. Positions and relative intensities of hyperfine components are indicated by vertical solid lines. Notice that most spectra have been enlarged and offset in $T_{MB}$. Numbers to the right indicate scaling factors and offset values. The vertical dashed lines show the velocity range of bulk CO emission.

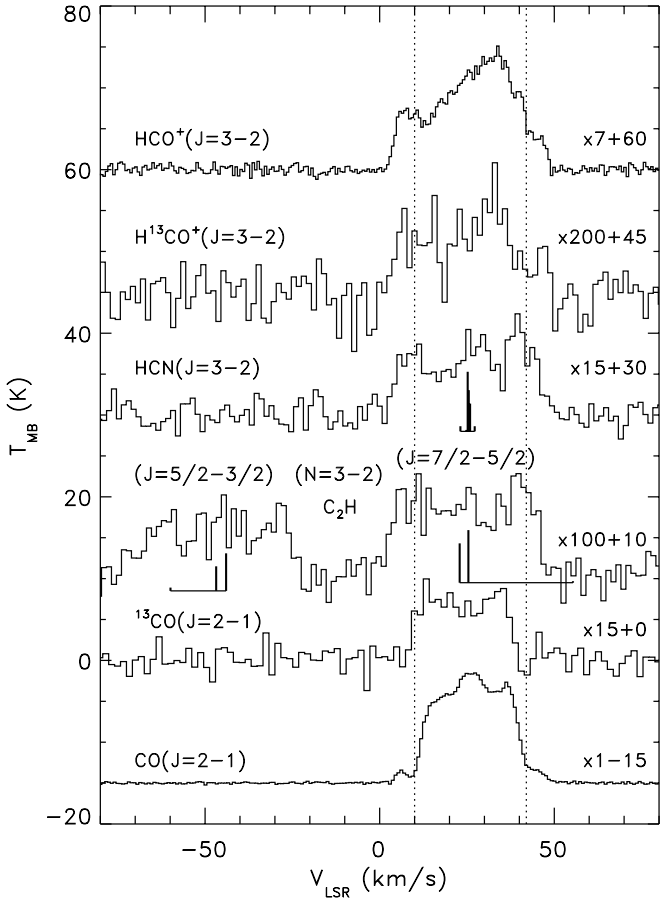


FIG. 2.—200 GHz band spectra at the central position of NGC 7027. See Fig. 1 for explanations.

not been detected in NGC 7027 in other frequency bands (Vallée et al. 1990), and we assume no C26α emission near He26α. The model recombination line profiles are shown in Figure 4. When the model H26α and He26α profiles were subtracted from the observation, there was a recognizable amount of residual at the expected velocity of $CO^+$ ($N = 3$–2, $J = 5/2$–$3/2$). Gaussian fits to the residual and the $J = 7/2$–$5/2$ component under the fixed line velocities and a common line width show that the two fine-structure components have relative intensities close to the theoretical value. Unfortunately, the line widths of He recombination lines are not well constrained, ranging from 36 to 45 km $s^{-1}$ (Vallée et al. 1990). Quantitatively, the residual is sensitive to the assumed line width of He26α. Qualitatively, however, there is little doubt about the presence of $CO^+$ ($N = 3$–2, $J = 5/2$–$3/2$).

The $HCS^+$ (6–5) spectrum, when binned to a frequency resolution of 10 MHz (11.7 km $s^{-1}$), shows a relatively narrow line at the expected radial velocity of 26 km $s^{-1}$ (Fig. 3). A search for a second rotational line $J = 8$–7 in the 300 GHz band was unsuccessful (also in Fig. 3). We have not had an opportunity to check whether the 26 km $s^{-1}$ feature in the 200 GHz band spectrum arose from a line in the mirror sideband or an unrelated cloud. A further confirmation is necessary to assign the apparent feature in the 200 GHz spectrum to $HCS^+$ (6–5) at 256.0278 GHz. If the 256 GHz feature is actually $HCS^+$ (6–5), the 3 $\sigma$ upper limit to the $HCS^+$ (8–7) line corresponds to $T_{ex} < 25$ K. In spite of long integrations, we did not detect $H_3O^+$, $HCNH^+$, $SO^+$, or CS (Fig. 3).

### 2.2. *Spectral Characteristics*

The observed spectra in Figure 1 (300 GHz) are generally wider in FWHM than those of CO (3–2) and $^{13}CO$ (3–2) observed at the same beam size. A similar trend is clearly recognizable in Figure 2 (200 GHz). The bulk CO emission occurs in the central velocity range between 10 and 42 km $s^{-1}$ in $V_{LSR}$ (indicated by dashed lines in Figures 1 and 2), whereas the other species show emission clearly outside the central velocity range. Even though $C_2H$ and CN have hyperfine components several kilometers per second apart, the excess line widths clearly exceed the separations of major hyperfine components shown in Figures 1 and 2. The relatively large widths of HCN (1–0) have already been noted in early studies by Sopka et al. (1989) and Deguchi et al. (1990) in comparison with CO (1–0). The $HCO^+$ (1–0) spectrum in Deguchi et al. (1990) shows fast components in absorption against continuum from the ionized region. The actual velocity extent at zero intensity (FWZI) is more clearly seen in the higher rotational lines of $HCO^+$. The present observations show that not only $HCO^+$ and HCN but also $CO^+$, CN, $C_2H$, and even $H^{13}CO^+$ have line widths larger than that of the bulk CO emission. The wide line widths seem common in many molecules in NGC 7027, and CO and $^{13}CO$ rather seem exceptions to the trend.

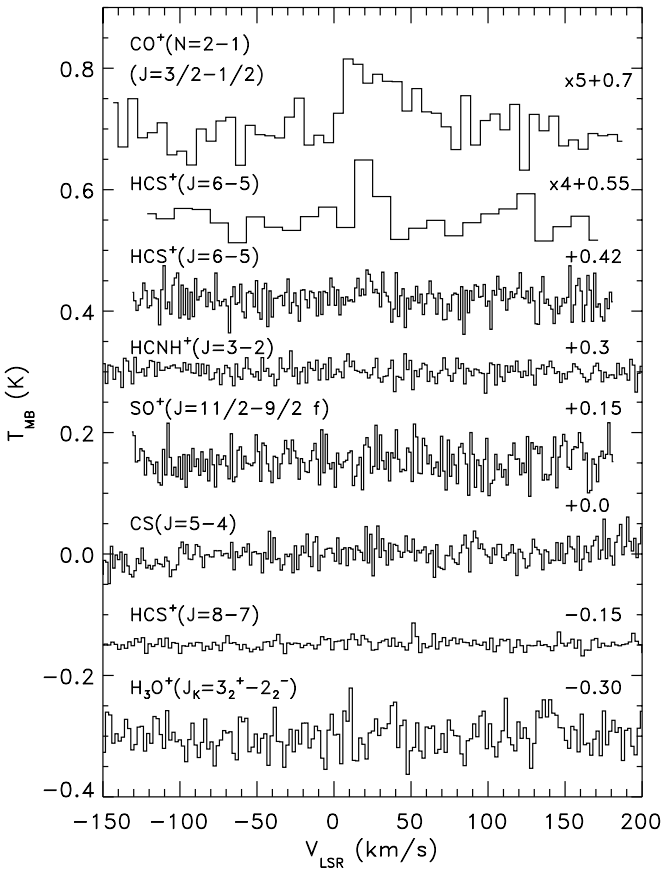


FIG. 3.—Weak lines and negative results in NGC 7027. The two plots for $HCS^+$ ($J = 6$–5) are from the same data but are presented at different velocity resolutions.

A closer inspection of the profiles in Figures 1 and 2 reveals that CO has weak fast components outside the central velocity range and that the FWZI is about 50 km $s^{-1}$, almost identical to those of $HCO^+$, $H^{13}CO^+$, HCN, CN, and $C_2H$. The $^{13}CO$ (2–1) profile does not show such fast components possibly because of poor signal-to-noise ratio (S/N). The $^{13}CO$ (3–2) shows a fast blue component. The fast but weak CO emission has been detected and discussed by Jaminet et al. (1991). The fast CO components are also recognizable in the CO (1–0) interferometric observations (in their position-velocity maps in particular) by Bieging et al. (1991) and Graham et al. (1993).

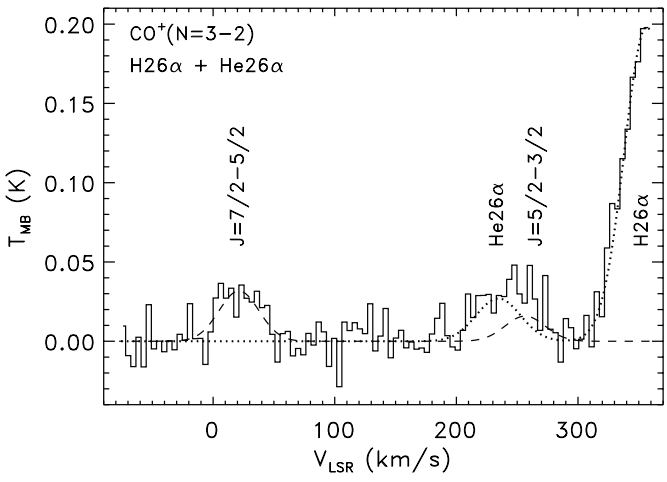


FIG. 4.—$CO^+$ ($N = 3$–2, $J = 7/2$–5/2, and $J = 5/2$–3/2), H26α, and He26α in NGC 7027.

The intensities of the fast CO components relative to that of the bulk CO emission increase progressively in higher $J$ transitions or with smaller beams. The fast CO components, therefore, must have small sizes (or volumes) and possibly relatively high gas temperatures compared with the rest of the CO emitting region (or volume). Indeed, CO (1–0) observations by Bieging et al. (1991) and Graham et al. (1993) clearly show that the $V_{LSR} < 10$ km $s^{-1}$ and the $V_{LSR} > 42$ km $s^{-1}$ components have sizes of 5″–10″. Jaminet et al. (1991), from profile fitting, conclude that the fast CO emission must originate from the innermost part of the neutral envelope of NGC 7027.

The fast components in the other observed species are relatively strong in comparison with the components in the central velocity range (hereafter the slow components) of the respective species. The fast components in $HCO^+$ (3–2, 4–3), HCN (3–2, 4–3), and CN ($N = 3$–2, $J = 7/2$–5/2) have spectral shapes clearly different or separable from those of the slow components. As will be discussed later, the angular offsets and sizes of the fast components of $HCO^+$, CN, and HCN are similar to those of the fast CO components.

From the spectra taken at one position, it is difficult to estimate where the emission for the slow components originates from. If the fast components correspond to a small, expanding spherical shell or torus, the apparent slow components could originate from the tangentially (with respect to the line of sight) moving part of the fast components. Alternatively, the slow components may simply arise from part of the slowly ($\sim 15$ km $s^{-1}$) expanding neutral envelope, the remnant of the CSE during the asymptotic giant branch (AGB) phase. In either case, if the observed lines are optically thin and if the emitting volume corresponding to the central velocity range of the spectra is similar to that of CO, then the spectra would resemble that of CO or at least $^{13}CO$. This is clearly not the case. For example, both the CO and $^{13}CO$ spectra lack the prominent narrow features at 40 km $s^{-1}$ commonly present in the HCN (4–3, 3–2), CN (3–2, 7/2–5/2), $C_2H$ ($N = 4$–3, $J = 9/2$–7/2 and $N = 3$–2, $J = 7/2$–5/2), and (although less prominent) $HCO^+$ (4–3) spectra. Most of the HCN, CN, and $C_2H$ emission must originate from the gas or volume that is inconspicuous in CO spectra. Such gas is likely to have a small volume or a small angular extent compared with the entire CO envelope of NGC 7027 and is likely to contribute little to the total CO emission from NGC 7027.

### 2.3. *Maps*

Channel maps in $HCO^+$ (4–3) are shown in Figure 5. The $HCO^+$ (4–3) maps are consistent with the interferometric observation in $HCO^+$ (1–0) by Likkel (1992) over the central velocity range ($10 < V_{LSR} < 42$ km $s^{-1}$). The fast blue ($V_{LSR} < 10$ km $s^{-1}$) and fast red ($V_{LSR} > 42$ km $s^{-1}$) components in Figure 5 have their emission centers offset from the map center to the north and south, respectively, by about 5″. $HCO^+$ (3–2) channel maps (not presented in this paper) show emission distributions similar to $HCO^+$ (4–3). Figure 6 shows position-velocity maps in $HCO^+$ (4–3). The positional offsets of the fast components are clearly seen in the declination-velocity map (Fig. 6*a*), whereas there is no positional shift of the fast components in the right ascension–velocity map (Fig. 6*b*). Gaussian deconvolution

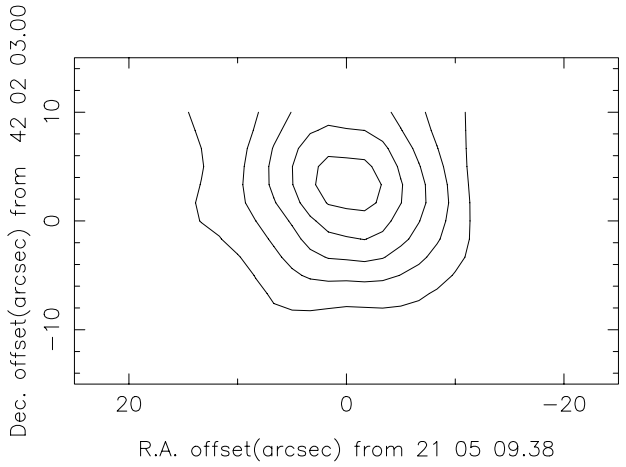


Fig. 5*a*

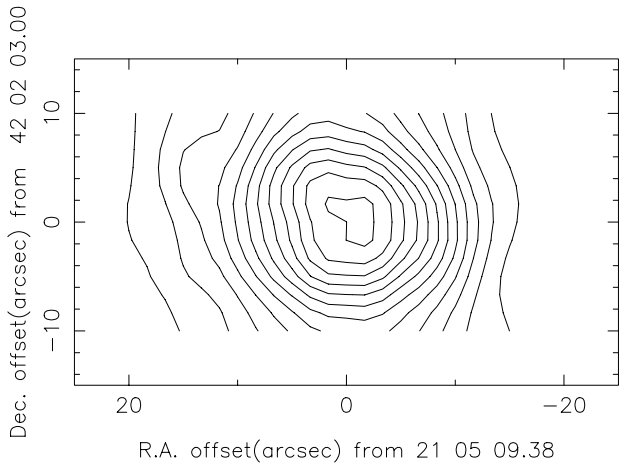


Fig. 5*b*

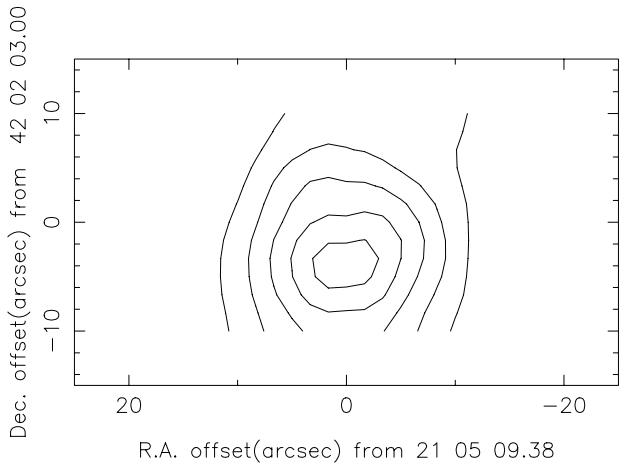


Fig. 5*c*

FIG. 5.—Channel maps in $HCO^+$ ($J = 4$–3). (*a*) Fast blue component ($-2$ to 8 km s$^{-1}$). (*b*) Slow component (8–42 km s$^{-1}$). (*c*) Fast red component (42–50 km s$^{-1}$). Contours represent average $T_{MB}$ over the velocity range. The lowest contour is 0.1 K, and the contour interval is 0.15 K.

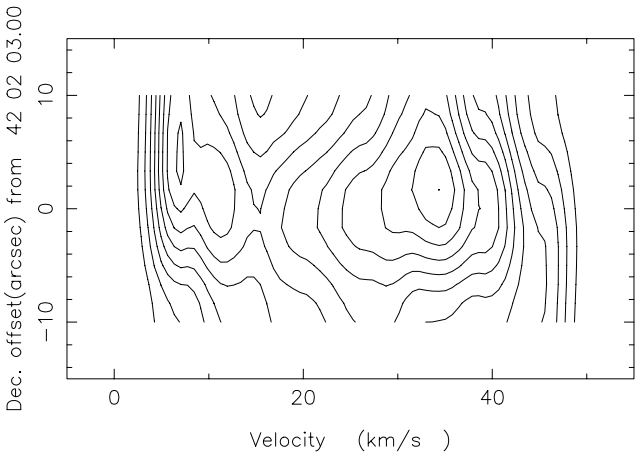


Fig. 6*a*

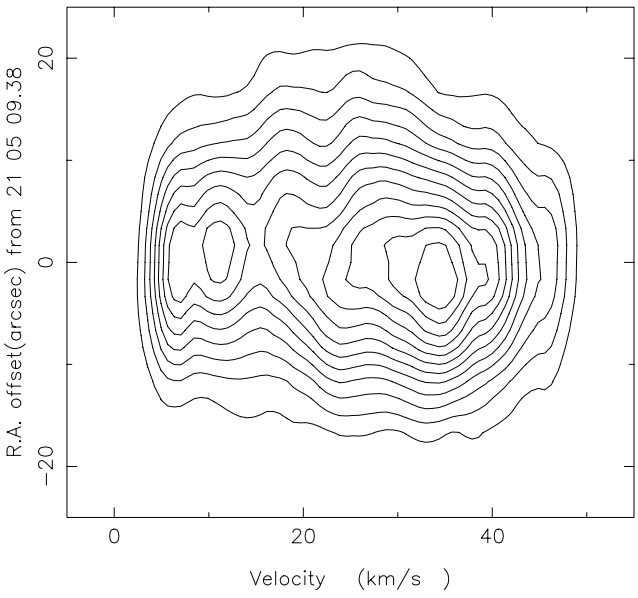


Fig. 6*b*

FIG. 6.—(*a*) Declination-velocity map in $HCO^+$ ($J = 4$–3) at $\Delta\alpha = 0''$. (*b*) Right ascension–velocity map in $HCO^+$ ($J = 4$–3) at $\Delta\delta = 0''$. The lowest contour and the contour interval are both 0.15 K in $T_{MB}$.

of the fast components suggests source sizes of order 7″ (§ 2.4).

The fast red component is not securely detected in $HCO^+$ (1–0) by Deguchi et al. (1992) or Likkel (1992). The fast blue component appears at 6 km s$^{-1}$ in Likkel (1992) and has a very small extent ($\sim 7''$) with its position offset by 5″ to the north from the source center.

Figure 7 shows channel maps in CN ($N = 3$–2, $J = 7/2$–5/2). The sampling interval is 7″, and the mapped area is $50'' \times 50''$. As indicated in Figure 1, major hyperfine components ($F = 9/2$–7/2, 7/2–5/2, 5/2–3/2) are close to each other in frequency (all within 1 km s$^{-1}$), so that velocity values in the channel maps directly reflect gas velocities. In fast blue ($V_{LSR} < 10$ km s$^{-1}$) and fast red ($V_{LSR} > 42$ km s$^{-1}$) channel maps, the emission centers are offset to the north and south, respectively, by about 5″, although the estimates are less accurate than in $HCO^+$ as a result of the 7″ sampling. The declination-velocity map (Fig. 8) confirms the positional shifts of the fast components.

Channel maps in HCN (4–3) are shown in Figure 9. The sampling interval is 10″, so that a reliable estimate of offset of emission of order 5″ cannot be made. Nevertheless, the fast blue and red channel maps show positional biases of

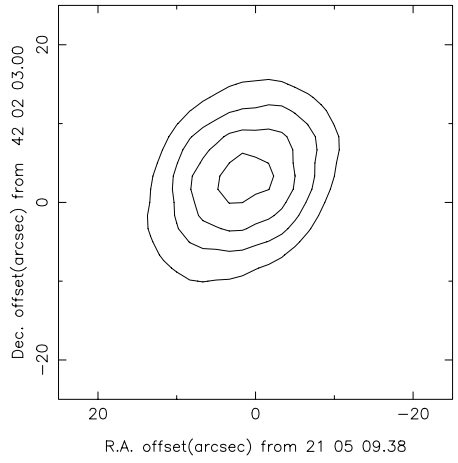


Fig. 7*a*

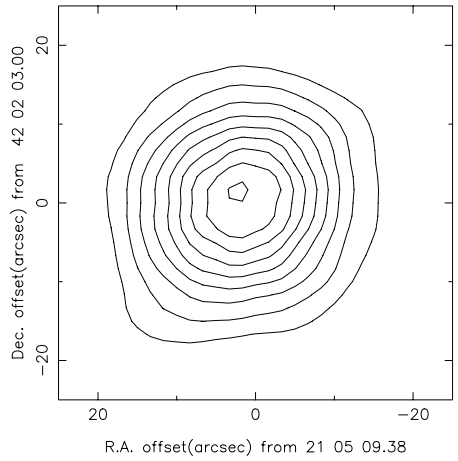


Fig. 7*b*

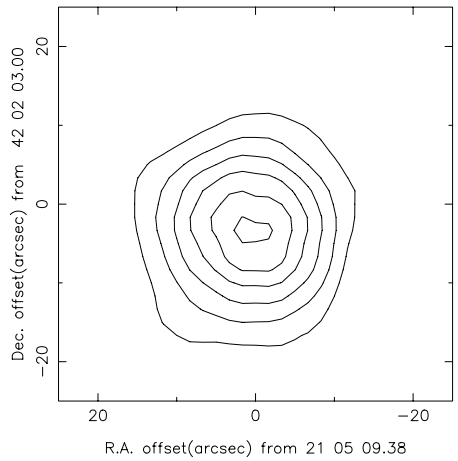


Fig. 7*c*

FIG. 7.—Channel maps in CN ($N = 3$–2, $J = 7/2$–5/2). (*a*) Fast blue component ($-1$ to 8 km s$^{-1}$). (*b*) Slow component (8–43 km s$^{-1}$). (*c*) Fast red component (43–48 km s$^{-1}$). Contours represent average $T_{MB}$ over the velocity range. The lowest contour is 0.1 K, and the contour interval is 0.07 K.

emission to the north and south, respectively. The positional shifts of the fast components are recognizable in the declination-velocity map (Fig. 10).

In all three molecules, we commonly see a positional shift to the north for the fast blue component and a shift to the

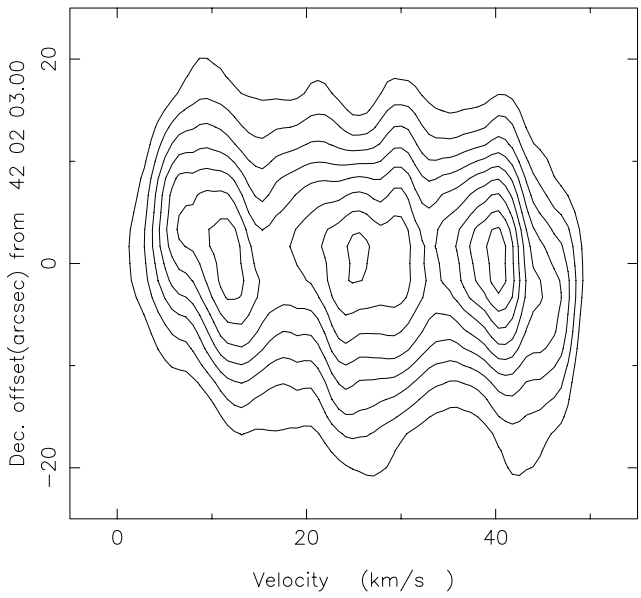


FIG. 8.—Declination-velocity map in CN ($N = 3$–2, $J = 7/2$–5/2). This is an average over $-10'' \leq \Delta\alpha \leq 10''$. The lowest contour is 0.1 K and the contour interval is 0.07 K in $T_{MB}$.

south for the fast red component. At least in one molecule ($HCO^+$), our maps are consistent with a high angular resolution study in a different transition. In addition, as will be shown in § 2.4, the fast components have sizes of order 7″.

The blue and red fast components are clearly seen in interferometric maps in CO (1–0) by Graham et al. (1993) and Bieging et al. (1991), particularly in their position-velocity maps. As hinted in the early CO (1–0) interferometric map by Masson et al. (1985), the later observations in the same line clearly show positional offsets of $\sim 5''$ of the fast blue and red CO (1–0) components to the north and south, respectively.

These semiquantitative coincidences in positional offsets and in size of the fast blue and red components of CO, CN, HCN, and $HCO^+$, together with the clear velocity coincidences discussed in § 2.2, are sufficient for us to assume that the blue fast components in the CO, CN, HCN, and $HCO^+$ (including $H^{13}CO^+$) spectra originate from the same blueshifted gas and that the red components originate from the same redshifted gas. Judging from the CO (1–0) observations mentioned above, the blue fast gas is located several arcseconds to the north and has a size of order 5″–10″. The red fast gas is located several arcseconds to the south and has a similar size. The velocity shifts for the fast components are, except for the signs, very similar at 16–26 km s$^{-1}$ with respect to the systemic velocity of $V_{LSR} = 26$ km s$^{-1}$. The clear positional offsets mean that the emitting gas does not have a spherically symmetric distribution.

The extents and locations of the fast components of the $C_2H$ and $CO^+$ emission are unclear, but it is reasonable for us to assume that $C_2H$ and $CO^+$ emission also originates from the same fast gas that is responsible for the emission of the mapped molecules.

### 2.4. *Source Size*

Since the spectral shapes of the observed molecules are very different from those of CO, high-resolution maps in CO (1–0) are a poor guide for the size and distribution of the emitting regions of these molecules, especially in the

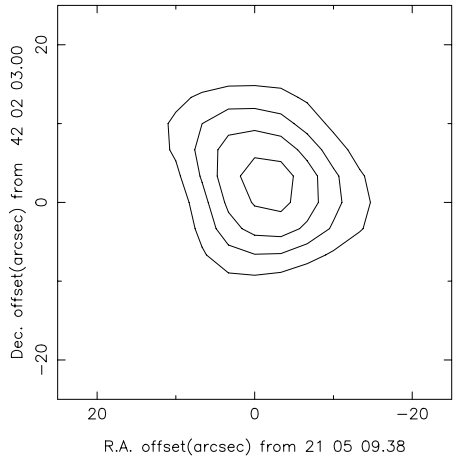


Fig. 9*a*

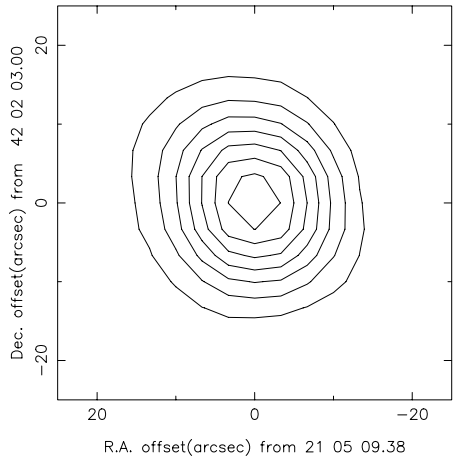


Fig. 9*b*

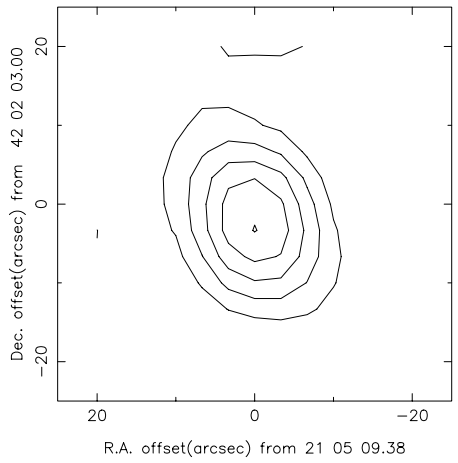


Fig. 9*c*

FIG. 9.—Channel maps in HCN ($J = 4$–3). (*a*) Fast blue component (0–8 km s$^{-1}$). (*b*) Slow component (8–44 km s$^{-1}$). (*c*) Fast red component (44–49 km s$^{-1}$). Contours represent average $T_{MB}$ over the velocity range. The lowest contour is 0.1 K, and the contour interval is 0.07 K.

central velocity range. The source is not well resolved in our best sampled map in $HCO^+$. We estimate the average source size for the integrated emission by assuming a circular Gaussian source coupled to a Gaussian beam. The integrated intensities normalized by that of the central position

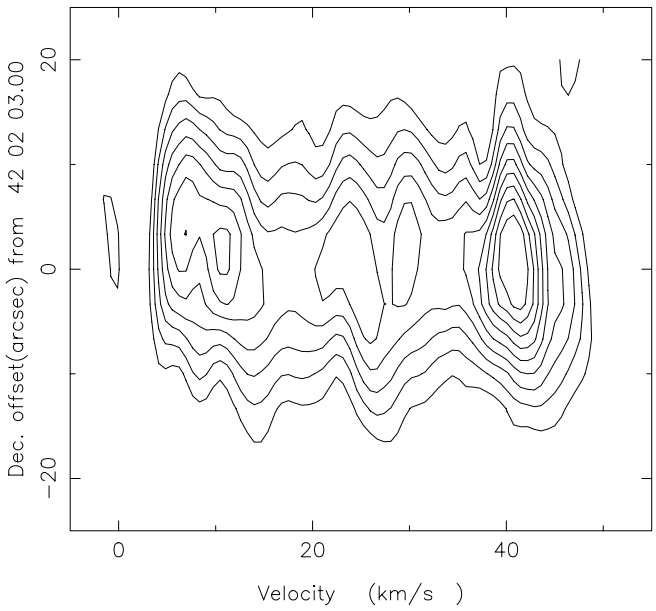


FIG. 10.—Declination-velocity map in HCN ($J = 4$–3). This is an average over $-10'' \leq \Delta\alpha \leq 10''$. The lowest contour is 0.1 K and the contour interval is 0.07 K in $T_{MB}$.

are plotted with respect to the angular offsets, and the plots are fitted with a model intensity distribution expected from Gaussian source–Gaussian beam coupling. The source size estimates are made separately for the $HCO^+$ (4–3, 3–2), HCN (4–3), and CN (3–2) maps.

The results are shown in Figures 11–14. A Gaussian source with a diameter of 13.″2 (FWHM) gives the best fit to the $HCO^+$ (4–3) distribution. The 13.″2 source model gives reasonable fits to the distributions of emission in the other maps, although the fits are not necessarily the best in individual maps. The source size is clearly smaller than 20″ in any of the mapped lines. We adopt the source size of 13.″2 common to all the observed lines except CO and $^{13}CO$. This source model will be used to convert $T_{MB}$ to the radiation temperature $T_R$ ($= T_{MB}/f_C$) and to correct line ratios in excitation analysis (§ 3). The beam coupling factor $f_C$ against

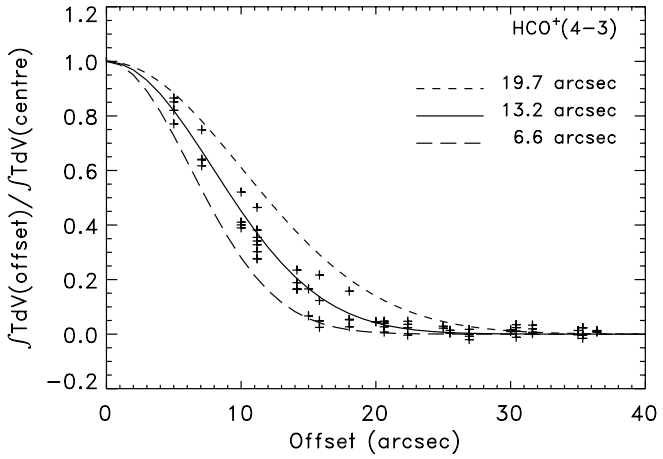


FIG. 11.—Observed and model flux distributions with respect to angular offsets. Crosses represent observed integrated temperatures normalized at the central position. Curves represent model flux distributions expected from Gaussian sources. The half-peak diameter in arcseconds of a Gaussian source assumed in each model is indicated in the figure.

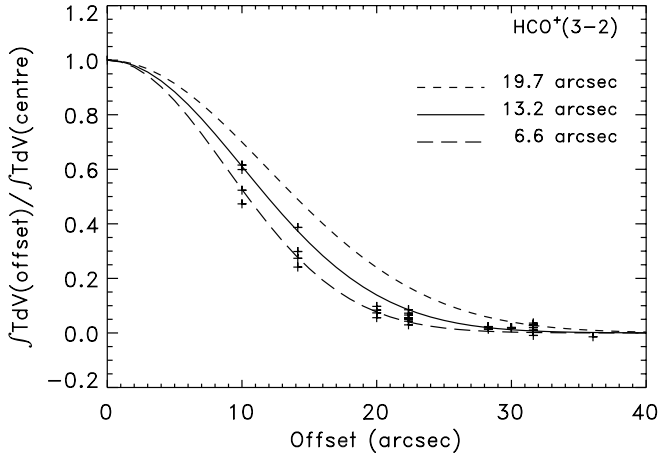


FIG. 12.—Observed and model flux distributions for $HCO^+$ ($J = 3$–2)

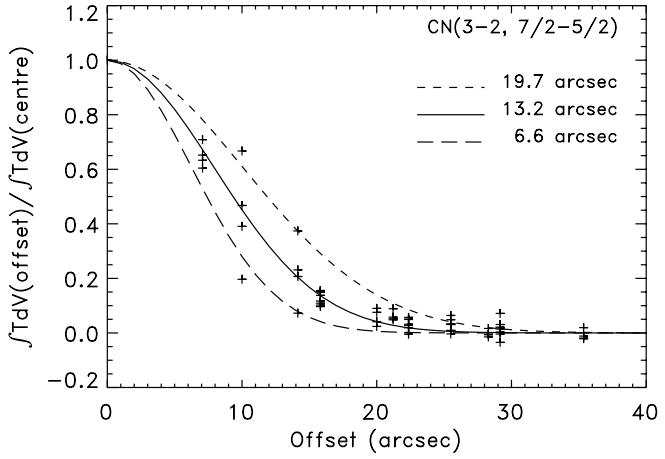


FIG. 13.—Observed and model flux distributions for CN ($N = 3$–2, $J = 7/2$–5/2).

the Gaussian source is 0.31 for the 200 GHz lines and 0.50 for the 300 GHz lines.

Bachiller et al. (1997) observed the CN (3–2, 7/2–5/2) line in NGC 7027 with the 10 m telescope (22″ beam) at the Caltech Submillimeter Observatory (CSO). Against the adopted 13.″2 source, $\int T_{MB}\,dV = 17.9$ K km s$^{-1}$ (CSO) translates to $\int T_R\,dV = 67.6$ K km s$^{-1}$ (CSO). Our measurement of the same line with the JCMT (Table 1) corresponds to $\int T_R\,dV = 70.0$ K km s$^{-1}$, an excellent agreement. Bachiller et al. (1997) also measured $HCO^+$ (3–2) in NGC 7027 with the IRAM 30 m telescope (12″ beam). Against the adopted 13.″2 Gaussian source, $\int T_{MB}\,dV = 76 \pm 5$ K km s$^{-1}$ (IRAM) translates to $\int T_R\,dV = 139 \pm 9$ K km s$^{-1}$ (IRAM). Our $HCO^+$ (3–2) measurement in Table 1 (19.″7 beam) corresponds to $\int T_R\,dV = 179$ K km s$^{-1}$. The 30% discrepancy is slightly larger than in CN but still acceptable because the beam of IRAM is small with respect to the source size and the IRAM measurement may reflect inhomogeneity of emission over the source. If the IRAM has a beam size of 9″ at 267 GHz, however, the discrepancy is 40% . These comparisons suggest that the 13.″2 Gaussian source model is a good representation of the emitting

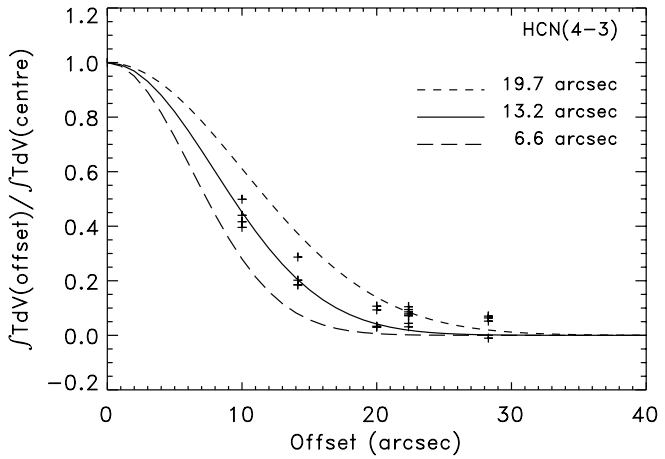


FIG. 14.—Observed and model flux distributions for HCN ($J = 4$–3)

regions of the observed rotational lines of various species other than CO and $^{13}CO$.

Attempts have also been made to constrain the source sizes of the fast components of $HCO^+$ (4–3), CN (3–2), and

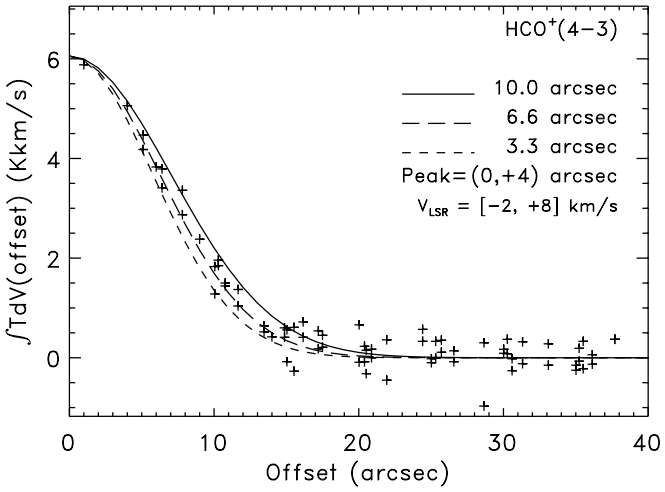


Fig. 15*a*

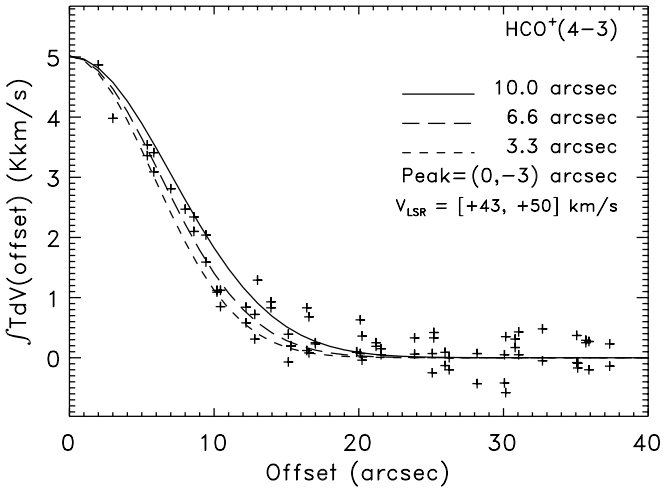


Fig. 15*b*

FIG. 15.—Observed and model flux distributions for the fast (*a*) blue and (*b*) red components of $HCO^+$ ($J = 4$–3). Crosses represent observed integrated temperatures. The assumed parameter values are indicated in the figures, where the free parameters are the offsets ($\Delta\delta$, $\Delta\alpha$), the source size, and the peak integrated intensity. The velocity ranges are indicated in the figures.

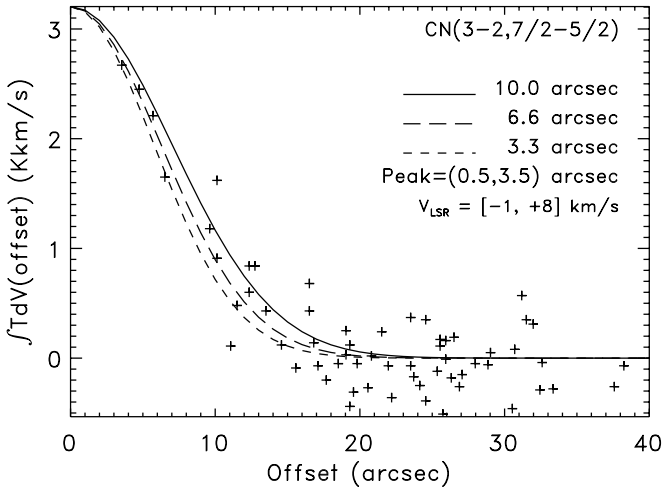


Fig. 16*a*

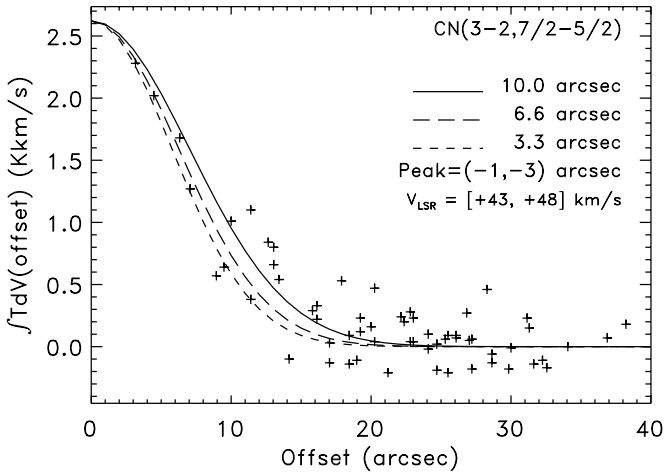


Fig. 16*b*

FIG. 16.—Observed and model flux distributions for the fast (*a*) blue and (*b*) red components of CN ($N = 3$–2, $J = 7/2$–5/2)

HCN (4–3) with four free parameters for a Gaussian source: the source size, the peak flux, and the peak position ($\Delta\alpha$, $\Delta\delta$). Figure 15 shows the results of Gaussian deconvolution for the fast blue and red components of $HCO^+$ (4–3). The deconvolved size for the fast blue component is between 3″ and 10″ with a source position of (0″, 4″). The fast red component has a size between 3″ and 10″ with a source position of (0″, −3″). Our size estimates are thus 7″ ± 4″ for both fast components of $HCO^+$. Because of sparse sampling, CN or HCN observations do not strongly constrain the source sizes and positions of the fast components except that the source sizes are smaller than 13″ and that the blue and red components are located to the north and south, respectively, of the center as discussed in § 2.3 (Figs. 16 and 17). However, a source model with a size of 7″ (from the $HCO^+$ fit) gives good fits to the CN fast components. A 10″ model gives reasonable fits to the HCN fast components as can be seen in Figure 17. We suggest a common source size of 7″ ± 4″ for the fast blue and red components of the three molecules.

## 3. ANALYSIS

### 3.1. *Line Ratios and Radiation Temperature*

The excitation analysis is carried out on the data at the central position only. The observed quantities that constrain excitation models are (1) the ratio of integrated intensities and (2) the peak radiation temperature. A summary is given in Table 2 of the utilized transitions and observed values. Details of the estimating process of these parameter values are discussed below.

We have observations in two rotational transitions for $HCO^+$, $H^{13}CO^+$, $CO^+$, $C_2H$, and HCN and in one rotational transition for CN.

The 300 and 200 GHz observations of $CO^+$ and HCN, all at the central position, were corrected for the beam coupling factors against the estimated 13″.2 source. The ratio is taken between the integrated intensities in the present analysis. The higher rotational line is divided by the lower rotational line. The line intensity, however, is estimated from the highest $T_{MB}$ in a spectrum in Table 1 by

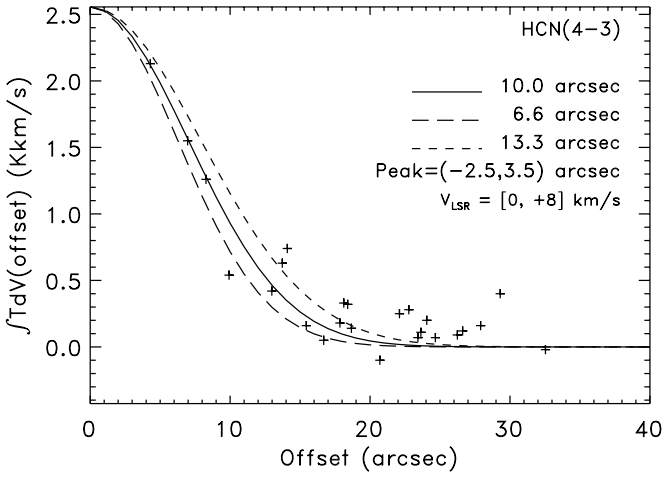


Fig. 17*a*

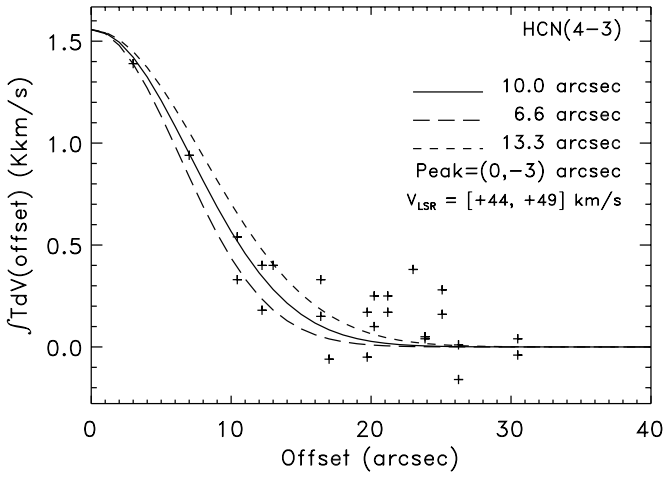


Fig. 17*b*

FIG. 17.—Observed and model flux distributions for the fast (*a*) blue and (*b*) red components of HCN ($J = 4$–3)

TABLE 2

LINE RATIOS AND DENSITY ESTIMATES

| PARAMETER | SPECIES | | | | | |
|---|---|---|---|---|---|---|
| | $HCO^+$ | $H^{13}CO^+$ | $CO^+$ | HCN | CN | $C_2H$ |
| Transitions: | | | | | | |
| (numerator) ..... | $J = 4–3$ | $J = 4–3$ | $N = 3–2$ $J = 7/2–5/2$ | $J = 4–3$ | $N = 3–2$ $J = 7/2–5/2$ | $N = 4–3$ $J = 9/2–7/2$ |
| (denominator) ..... | $J = 3–2$ | $J = 3–2$ | $N = 2–1$ $J = 3/2–1/2$ | $J = 3–2$ | $N = 2–1$ $J = 5/2–3/2$ | $N = 3–2$ $J = 7/2–5/2$ |
| Ratio (error %) ..... | 0.79 (±14) | 0.78 (±20) | 0.88 (±24) | 0.70 (±15) | 0.91 (±14) | 1.31 (±15) |
| $T_R$(numerator) (K) ..... | 4.68 | 0.123 | 0.063 | 1.96 | 2.60 | 0.64 |
| $T_k$ = 800 K Cases with Electron and Neutral Collisions | | | | | | |
| $n_H$ ($cm^{-3}$) ..... | 5.0E5 | 4.6E5 | 1.3E5 | 5.0E5 | 2.6E5 | 3.2E5 |
| $n_H$range ($cm^{-3}$) ..... | 3.8–6.7E5 | 3.0–7.1E5 | 0.8–2.0E5 | 3.8–6.7E5 | 2.0–3.5E5 | 2.2–5.0E5 |
| $\tau$(numerator) ..... | 0.35 | 0.0098 | 0.013 | 0.18 | 0.24 | 0.013 |
| $T_{ex}$(nume.) (K) ..... | 22.6 | 19.6 | 11.4 | 18.0 | 18.3 | 59.2 |
| $N/\Delta V$ ($cm^{-2}$ $km^{-1}$ s)..... | 2.2E12 | 5.7E10 | 1.7E11 | 1.9E12 | 1.3E13 | 1.1E13 |
| $X$ [$=n(i)/n_H$]..... | 1.5E−9 | 4.0E−11 | 4.3E−10 | 1.2E−9 | 1.7E−8 | 1.1E−8 |
| $N$ ($cm^{-2}$)..... | 6.5E13 | 1.7E12 | 6.5E12 | 4.3E13 | 3.5E14 | 2.4E14 |
| $T_k$ = 50 K Cases with Electron and Neutral Collisions | | | | | | |
| $n_H$ ($cm^{-3}$) ..... | 6.6E5 | 6.2E5 | 1.7E5 | 7.1E5 | 4.0E5 | >1.4E6 |
| $n_H$range ($cm^{-3}$) ..... | 4.3–10.2E5 | 4.0–9.5E5 | 1.1–2.6E5 | 5.0–8.8E5 | 3.0–5.3E5 | 1.4E6 |
| $\tau$(numerator) ..... | 0.39 | 0.0096 | 0.014 | 0.18 | 0.25 | <0.019 |
| $T_{ex}$(nume.) (K) ..... | 22.2 | 20.1 | 11.2 | 18.3 | 17.7 | >38.0 |
| $N/\Delta V$ ($cm^{-2}$ $km^{-1}$ s)..... | 2.5E12 | 6.0E10 | 1.7E11 | 2.0E12 | 1.4E13 | 1.1E13 |
| $X$ [$=n(i)/n_H$]..... | 1.2E−9 | 3.2E−11 | 3.2E−10 | 9.1E−10 | 1.1E−8 | <2.6E−9 |
| $N$ ($cm^{-2}$)..... | 7.4E13 | 1.8E12 | 6.5E12 | 4.7E13 | 3.7E14 | 2.4E14 |
| $T_k$ = 800 K Cases with Neutral Collisions Only | | | | | | |
| $n_H$ ($cm^{-3}$) ..... | 8.2E5 | 8.2E5 | 1.5E5 | 1.6E6 | 4.6E5 | 3.7E5 |
| $n_H$range ($cm^{-3}$) ..... | 5.3–12.7E5 | 5.0–12.7E5 | 0.6–2.6E5 | 1.1–2.3E6 | 3.5–6.2E5 | 2.6–5.7E5 |
| $\tau$(numerator) ..... | 0.38 | 0.0095 | 0.013 | 0.18 | 0.23 | 0.013 |
| $T_{ex}$(nume.) (K) ..... | 22.2 | 20.1 | 11.4 | 18.1 | 18.3 | 58.5 |
| $N/\Delta V$ ($cm^{-2}$ $km^{-1}$ s)..... | 2.4E12 | 5.7E10 | 2.0E11 | 2.1E12 | 1.3E13 | 1.1E13 |
| $X$ [$=n(i)/n_H$]..... | 9.4E−10 | 2.3E−11 | 4.5E−10 | 4.4E−10 | 9.4E−9 | 9.5E−9 |
| $N$ ($cm^{-2}$)..... | 7.0E13 | 1.7E12 | 7.8E12 | 5.0E13 | 3.5E14 | 2.4E14 |
| $T_k$ = 50 K Cases with Neutral Collisions Only | | | | | | |
| $n_H$ ($cm^{-3}$) ..... | 3.0E6 | 3.0E6 | 5.3E5 | 7.1E6 | 1.7E6 | >2.1E6 |
| $n_H$range ($cm^{-3}$) ..... | 1.9–5.0E6 | 1.8–5.0E6 | 3.2–8.8E5 | 5.0–10.2E6 | 1.2–2.2E6 | 2.1E6 |
| $\tau$(numerator) ..... | 0.40 | 0.0099 | 0.013 | 0.18 | 0.24 | <0.019 |
| $T_{ex}$(nume.) (K) ..... | 22.1 | 20.3 | 11.3 | 18.5 | 18.5 | >38.0 |
| $N/\Delta V$ ($cm^{-2}$ $km^{-1}$ s)..... | 2.5E12 | 6.0E10 | 1.7E11 | 2.0E12 | 1.4E13 | 1.1E13 |
| $X$ [$=n(i)/n_H$]..... | 2.8E−10 | 6.5E−12 | 1.0E−10 | 9.1E−11 | 2.7E−9 | <1.7E−9 |
| $N$ ($cm^{-2}$)..... | 7.5E13 | 1.8E12 | 6.5E12 | 4.7E13 | 3.7E14 | 2.4E14 |

NOTE.—$n_H = n(H) + 2n(H_2)$ and $n(H) = n(H_2)$. In addition to H and $H_2$, He with $n(He) = 0.1n_H$ contributes to neutral collisions. For electron collisions, $n(e) = 1 \times 10^{-3} n_H$ is assumed.

$T_R = T_{MB}/f_C$. Although we have a good estimate of the overall source size, the emitting region may consist of unresolved small clumps or filaments with a relatively small volume filling factor. Our $T_R$ estimates are, therefore, in a very strict sense, lower limits to actual $T_R$ values. In order to minimize the possibility of underestimating, we choose the highest $T_R$ in a spectrum. The source sizes estimated by Gaussian deconvolution at the peak velocity range from 10″ (CN 3–2) at 40 km $s^{-1}$ to 13″ ($HCO^+$ 4–3) at 35 km $s^{-1}$. The peak $T_R$ in the present work may therefore be underestimated by up to 40%.

In estimating the line ratio for $HCO^+$, $H^{13}CO^+$, and $C_2H$, we did not correct the 300 GHz spectra for the coupling factors. Instead, the $HCO^+$ (4–3) spectra at nine positions on and around the central position were convolved to an emulated spectrum matching the 19.″7 beam of the $HCO^+$ (3–2) observation. Likewise, the five-point maps in $H^{13}CO^+$ (4–3) and $C_2H$ (4–3) taken at the 5″ interval were convolved to spectra matching the beam size of the lower transitions. Then, $\int T_{MB}\, dV$ of the convolved spectrum was divided by that of the lower transition (listed in Table 1). Without an assumption on source distribution, the line ratios for $HCO^+$, $H^{13}CO^+$, and $C_2H$ are the most reliable in Table 2. The peak $T_R$ was estimated by correcting $T_{MB}$(4–3) in Table 1 for the beam coupling factor (without convolution) for $HCO^+$, $H^{13}CO^+$, and $C_2H$.

We only have the $N = 3–2$ observation for CN with the 13.″2 beam. Bachiller et al. (1997) have made an observation

of the $N = 2$–1 transition of these molecules with the IRAM 30 m telescope (12″ beam), and we use their observation. Since the CN $N = 2$–1, $J = 5/2$–3/2 hyperfine group is a well-defined emission feature, we adopt $\int T_{MB}\,dV$ for $J = 5/2$–3/2 by Bachiller et al. (1997) for our analysis. The matching hyperfine group in our data is CN $N = 3$–2, $J = 7/2$–5/2. Only the spectrum at the central position is used. The integrated intensities were corrected for respective beam coupling factors against the model 13″.2 source. The peak $T_R$ was similarly estimated from the peak $T_{MB}$ in Table 1.

### 3.2. *Large Velocity Gradient Excitation Analysis*

We use the large velocity gradient (LVG) formalism for a single, spherically symmetric zone (see, e.g., Goldreich & Kwan 1974) for photon escape probability. We assume an expanding spherical shell with an expansion speed of 26 km $s^{-1}$ and a radius of 0.025 pc, corresponding to a nominal velocity gradient $dV/dr$ of 1000 km $s^{-1}$ $pc^{-1}$. The assumed parameter values are based on the observed line width (FWZI) of 50 km $s^{-1}$ and the source size of 13″ (= 0.05 pc at a distance of 800 pc). Only those rotational levels in the ground vibrational state are considered, but sufficiently high rotational levels are included corresponding to assumed gas temperatures. The background radiation field is assumed to be the 2.7 K cosmic background radiation field. The nebular and dust continuum is not considered as a background radiation field. The omission may result in overestimates in density.

A set of statistical equilibrium equations are solved under a set of parameter values: (1) velocity gradient, (2) gas temperature $T_k$, (3) gas density $n_H$, (4) molecular column density $N$, and (5) fractional ionization $x_e$. For the first parameter, a common value of 1000 km $s^{-1}$ $pc^{-1}$ is assumed in all calculations. For the second parameter, two cases are considered: 50 and 800 K. For the fifth parameter, two cases are considered: $x_e = 0$ and $1 \times 10^{-3}$. The gas density and the molecular column density are determined based on the best fit to the observed line ratio and $T_R$(peak) under a given set of $T_k$ and $x_e$.

The statistical equilibrium calculations and model fits were carried out for $HCO^+$, $H^{13}CO^+$, $CO^+$, HCN, CN, and $C_2H$. Adopted molecular constants are described in the Appendix. For $CO^+$, HCN, CN, and $C_2H$, all fine and hyperfine sublevels (and transitions between sublevels) are separately treated. Overlapping of hyperfine components in HCN, CN, and $C_2H$ is not considered in the photon escape probability calculations under the assumption that the sum of optical depths of overlapping components does not exceed 1. For $HCO^+$, $H^{13}CO^+$, and $CO^+$, the ordinary LVG formalism should provide a good approximation for photon escape probability at any optical depth. Once the LVG iteration converged, the optical depths and intensities of relevant hyperfine components are added to obtain the overlapped optical depth and line intensity. As will be shown below, the optical depth of any of the observed lines in the present paper does not reach 1, unless $T_R$ is underestimated by a factor of 2–3.

The two gas temperatures have been chosen for the following considerations: (1) $T_K = 50$ K corresponds to the gas temperature at the base (innermost part) of the CO envelope (Jaminet et al. 1991), and (2) $T_K = 800$ K corresponds to the hot CO region responsible for high-$J$ CO lines detected with *ISO* (Liu et al. 1996). Theoretical studies predict gas temperatures of order 1000 K in a photodissociation region (also called the photon-dominated region or PDR; Sternberg & Dalgarno 1995; Natta & Hollenbach 1998; Yan et al. 1999). The hot CO region most likely corresponds to the PDR in NGC 7027, which is predicted to have enhanced abundances of newly formed molecules (Hasegawa et al. 2000; Yan et al. 1999; Sternberg & Dalgarno 1995).

In the present statistical equilibrium calculations, collisional excitations (and de-excitations) by electrons, He atoms, H atoms, and molecular hydrogen $H_2$ are considered. The rate constants for these collisional processes are discussed in the Appendix. As for the abundances of H, $H_2$, and He, half-molecular and half-atomic gas is assumed, i.e., $n(H) = n(H_2)$ in all cases, where $n(i)$ is the density of species $i$. The total hydrogen nucleus density is denoted by $n_H$ [$= n(H) + 2n(H_2)$]. The assumed helium abundance is 0.1, so that $n(He) = 0.1n_H$. The assumption of the half-molecular environment is more realistic than the conventional assumption of a fully molecular environment when molecular lines originate from a probable PDR region or a region very close to an H II region.

The rate constants for electron collisions are 3–4 orders of magnitude larger than those for $H_2$ collisions as illustrated in the Appendix. The inclusion of electron collisions is necessary because chemical models of PDR predict relative electron abundances close to the elemental carbon abundance (Sternberg & Dalgarno 1995; Yan et al. 1999; Hasegawa et al. 2000). Hasegawa et al. (2000) predict that more than 90% of carbon will be found as $C^+$ throughout the neutral envelope of NGC 7027, implying that the electron collisions cannot be ignored even in the extended CO envelope of NGC 7027. The inclusion of electron collisions introduces another uncertainty: the ionization degree $x_e$ [$= n(e)/n_H$]. Only two cases of fractional ionization are considered in the present work: (1) $x_e = 1 \times 10^{-3}$ based on the elemental carbon abundance of $1.26 \times 10^{-3}$ (Middlemass 1990), and (2) $x_e = 0$ to evaluate the uncertainty and effect of the introduction of electron collisions.

Thus, a total of four cases are considered, and density and column density estimates are made for each case. The results are presented in Table 2. In this table, "$n_H$ range" is estimated from the uncertainty in line ratio. The parameter $N/\Delta V$ (the molecular column density per unit velocity interval) is determined from the best fit to $T_R$(peak). The column density $N$ of a species is estimated by $N = (N/\Delta V)\Delta V^*$, with $\Delta V^* = \int T_R\,dV/T_R$(peak). Once $N/\Delta V$ and $n_H$ are determined, the density $n(i)$ of molecule $i$ and the relative molecular abundance $X(i)$ [$= n(i)/n_H$] are estimated from $N(i)/\Delta V = \Delta L X(i) n_H/\Delta V$ under the assumption $\Delta V/\Delta L = dV/dr$, where $\Delta L$ is the path length of the emitting region along the line of sight. Figures 18 and 19 are illustrative examples of the fitting procedure and the effects of electron collisions. In these figures, the $HCO^+$ observations (line ratio and $T_R$) are indicated by a thick horizontal bar. In each figure, three series of runs (corresponding to three cases of $N/\Delta V$) are shown, one of them passing through the observed parameter range.

In the 800 K case with electron and neutral collisions, the densities ($n_H$) estimated from five species range from 1.3 to $5.0 \times 10^5$ $cm^{-3}$. The optical depths $\tau$ for all lines in the 800 K case are less than 1, with the highest $\tau$ being 0.35 in $HCO^+$ (4–3). In the 50 K case with electron and neutral collisions, the density estimates are higher than in the 800 K

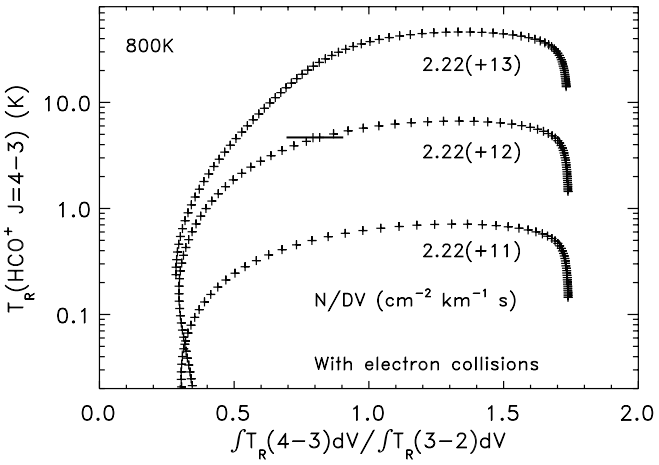


FIG. 18.—Observed and model line ratios with electron collision. A thick horizontal bar indicates the observed ratio HCO$^+$ (4–3)/(3–2) of integrated intensities (and uncertainty) and $T_R$(4–3)(peak) in the ratio-$T_R$ plane. Each cross represents an LVG model at a density. A sequence of crosses corresponds to models with the same column density of HCO$^+$. Shown here are the best-fit sequence and two sequences with HCO$^+$ column densities higher and lower by a factor of 10 than the best-fit column density. The lower left part corresponds to the lowest density and the right part to the highest density. Densities for adjacent crosses are different by 15%.

only by a factor of 1.5 or less. There is no solution for the central value for the observed ratio for $C_2H$ at 50 K, and the $C_2H$ results will be discussed separately in § 3.3. The optical depths are slightly higher in the 50 K case but still lower than 1, with the highest $\tau$ being 0.4 in HCO$^+$ (4–3). The estimated optical depths for the CN (3–2, 7/2–5/2) and HCN (4–3) lines are 0.25 and 0.18, respectively, even though $\tau$ of all the relevant hyperfine components have been combined. All other rotational transitions of HCN and CN are optically thin in the best-fit models. Therefore, our excitation calculations without consideration for hyperfine overlapping should not be introducing a serious error in the present estimates. The estimated densities from five species fall within a factor of about 4 in either the 50 K or the 800 K case with an exception of $C_2H$. In the electron collision cases, the estimated neutral densities $n_H$, $n$(H), $n(H_2)$, and

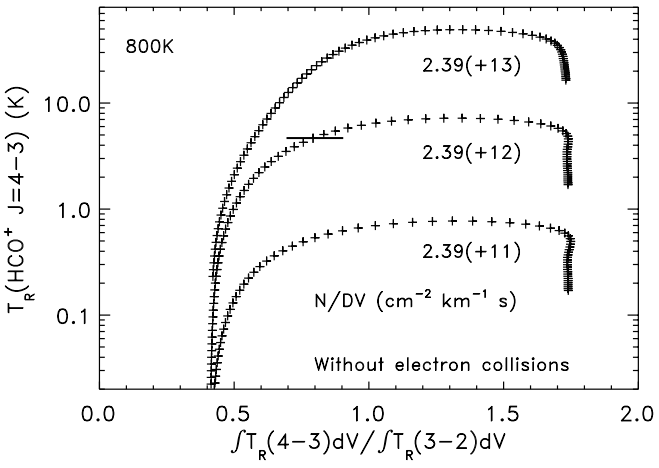


FIG. 19.—Observed and model line ratios without electron collision. Otherwise the same as Fig. 18.

$n$(He) are in large part surrogates of $n(e)$ because electron collisions dominate the collisional process and only $n(e)$ is effectively constrained. The electron collision rates are proportional to $A_{ul}\,v_{ul}^{-3}$ (see the Appendix). Therefore, similar excitation temperatures can occur to transitions of different molecules with very different dipole moments under the same electron density provided that the excitation energies are similar. For example, in low-density, optically thin limits, the excitation temperature for a two-level molecule can be approximated by $(g_u/g_l)\exp(-h_{ul}\,v/T_{ex}) = n_u/n_l = q_e(l \rightarrow u)n_e/A_{ul}$ (see the Appendix for notations). In this equation, $A_{ul}$ values in $q_e(l \rightarrow u)$ and the denominator cancel out, and the remaining factors that determine $T_{ex}$ have no or only a weak dependence on the dipole moment (see the Appendix).

In the 800 K case without electron collisions, the estimated densities are higher than in the 800 K case with electron collisions by factors of 1.2–3. Spreads in estimated density among five species are about a factor of 10. In the 50 K case without electron collisions, we see the highest density estimates in this work, ranging from $n_H \sim 5 \times 10^5$ (CO$^+$) to $7 \times 10^6$ cm$^{-3}$ (HCN). The highest $\tau$ is 0.4 (HCO$^+$). Thus, unless we have underestimated $T_R$ by more than a factor of 2, all observed lines are optically thin.

In many other studies, only $H_2$ collisions are assumed in the statistical equilibrium calculations. For comparison purposes, the estimates of $n_H$ in Table 2 (neutral-only cases) may be converted to equivalent values $n^*(H_2)$ expected under the $H_2$-only assumption through $n^*(H_2) = 0.88 n_H$.

From intensities of far-IR doublet lines of CH observed with *ISO*, Liu et al. (1997) estimate $n(H_2) \sim 10^5$ cm$^{-3}$ ($H_2$ collisions only). From CH$^+$ observations with *ISO*, however, Cernicharo et al. (1997) estimate $n(H_2) \sim 2$–$5 \times 10^7$ cm$^{-3}$ ($H_2$ collisions only) at $T_k = 300$–$500$ K. The density estimate will be lower by a factor of 2–3 if electron collisions are included (Cernicharo et al. 1997). Jaminet et al. (1991), based on CO excitation calculations and profile fitting, estimate $T_k = 50$ K and $n(H_2) \sim 5 \times 10^4$ cm$^{-3}$ ($H_2$ collisions only) at the innermost part of the CO envelope (Volk & Kwok 1997). Density estimates in our neutral-only case at 50 K are $n_H = 5$–$70 \times 10^5$ cm$^{-3}$, clearly higher than those from the CO analysis. Volk & Kwok (1997) constructed a model similar to the one by Jaminet et al. (1991) with a dense, hot shell [$n(H_2) = 9 \times 10^5$ cm$^{-3}$, $T_k = 800$ K]. The density estimates in the 800 K case with neutral collisions only are similar to those in the dense shell in Volk & Kwok (1997).

The column density estimates are not very sensitive to the assumptions in gas temperature and in fractional ionization. Our best estimates of molecular column densities for the emitting region are summarized in Table 3. The present estimate of $N(CO^+) \sim 7 \times 10^{12}$ cm$^{-2}$ supports the early estimate of $4 \times 10^{12}$ cm$^{-2}$ by Latter et al. (1993) under the LTE assumption at 200 K. The estimate of $3.5 \times 10^{14}$ cm$^{-2}$ for CN is in good agreement with $3 \times 10^{14}$ cm$^{-2}$ by Bachiller et al. (1997). Bachiller et al. (1997), however, estimate the total optical depth (the sum of optical depths of all the hyperfine components of a rotational transition of CN) for $N = 2$–1 to be 2. Our estimate of the total optical depth for $N = 2$–1 is from 0.17 (800 K) to 0.24 (50 K) both with electron collisions. Bachiller et al. (1997) conservatively estimate $N(HCN) > 4.5 \times 10^{13}$ cm$^{-2}$ on concern that the HCN lines may be optically thick. Our estimate is close to their lower limit. As stated above, the HCN lines are

TABLE 3

OBSERVED AND MODEL COLUMN DENSITIES FOR NGC 7027

| | OBSERVATION | | | MODEL 1[a] | | | MODEL 2[b] | | | |
|---|---|---|---|---|---|---|---|---|---|---|
| MOLECULE | $X$ | $N$ ($cm^{-2}$) | $N\Delta S$[c] | $X$ | $N$[d] ($cm^{-2}$) | $N\Delta S$[c] | $X$ | $N$[d] ($cm^{-2}$) | $N\Delta S$[c] | REF. |
| $CH^+$ ..... | ... | 2.5E14 | 7.8E47 | 3E−8 | 8.7E14 | 1.7E49 | 4E−8 | 1.1E15 | 1.0E49 | 1 |
| CH..... | ... | 3E16 | 1E50 | 7E−8 | 2.7E15 | 2.6E49 | 1.6E−7 | 2.4E15 | 2.3E49 | 2 |
| CO..... | ... | ... | 1.6E51 | 5E−4 | 3.2E20 | 3.1E53 | 5E−4 | 8.8E18 | 8.6E52 | 3 |
| SiO ..... | ... | <2.3E11 | ... | 6E−10 | 1.6E13 | 1.5E47 | 1.7E−9 | 2.2E13 | 2.1E47 | 4 |
| CS ..... | <2E−9 | <2.4E13 | ... | 1.7E−9 | 2.5E13 | 2.5E47 | 1.2E−9 | 8.4E12 | 8.2E46 | 5 |
| CS ..... | | <1.1E12 | | | | | | | | 4 |
| $CO^+$ ..... | 4.3E−10 | 6.5E12 | ... | 9E−10 | 2.0E13 | 1.9E47 | 1.6E−9 | 2.1E13 | 2.0E47 | 5 |
| $HCO^+$..... | 1.5E−9 | 6.5E13 | ... | 1.8E−9 | 4.6E13 | 4.3E47 | 5E−9 | 7.7E13 | 7.3E47 | 5 |
| CN..... | 1.7E−8 | 3.5E14 | ... | 1.1E−8 | 2.4E14 | 2.3E48 | 8E−9 | 6.8E13 | 6.6E47 | 5 |
| HCN ..... | 1.2E−9 | 4.3E13 | ... | 1.3E−8 | 1.8E14 | 1.7E48 | 6E−9 | 3.4E13 | 3.3E47 | 5 |
| $C_2H$ ..... | 1.1E−8 | 2.4E14 | ... | 8E−9 | 1.5E14 | 1.4E48 | 1.5E−8 | 1.2E14 | 1.2E48 | 5 |

[a] Hasegawa et al. 2000.
[b] $n_H$(Model 2) = 0.4$n_H$(Model 1).
[c] Total number of molecules in the source.
[d] Calculated by $\int n(i)4\pi r^2\,dr/\Delta S$, where $\Delta S$ is the projected source area.
[e] Calculated by $\int n(i)4\pi r^2\,dr$.
REFERENCES.—(1) Cernicharo et al. 1997. (2) Liu et al. 1997. (3) Liu et al. 1996. (4) Bachiller et al. 1997. (5) This paper.

probably optically thin in NGC 7027. Our estimate of $N(HCO^+) \sim 7 \times 10^{13}$ $cm^{-2}$ is in good agreement with $6.4 \times 10^{13}$ $cm^{-2}$ by Bachiller et al. (1997).

Our best estimate for the $HCO^+/H^{13}CO^+$ ratio is 40, similar to $\int T_{MB}(HCO^+ 3\text{–}2)dV/\int T_{MB}(H^{13}CO^+ 3\text{–}2)dV = 38$. The isotopomer ratio for this species in NGC 7027 is estimated for the first time. Bachiller et al. (1997) estimate $CO/^{13}CO > 25$ whereas Kahane et al. (1992) estimate $CO/^{13}CO = 65$ (or higher) in NGC 7027.

### 3.3. $C_2H$ *Analysis*

The $C_2H$ results are discussed in detail in this subsection. The observed line ratio $\int T_R(4\text{–}3, 9/2\text{–}7/2)dV/\int T_R(3\text{–}2, 7/2\text{–}5/2)dV$ for $C_2H$ is $1.31 \pm 0.19$, the central value of which cannot be attained at 50 K. The highest ratio at 50 K in the present models is about 1.245, which occurs in the LTE and optically thin regime with densities higher than $1 \times 10^6$ $cm^{-3}$. We encountered negative $T_{ex}$ for the lowest three rotational transitions in some models. Such weak masers commonly occur in model excitation calculations for simple molecules, and the highest line ratio still does not reach the observed value. The entries in Table 2 for $C_2H$ (50 K cases) correspond to the lower bound of the ratio.

We see no indication of an erroneous calibration during the observation. There are no hyperfine anomalies in observed intensity either. The observed ratio of $J = 7/2\text{–}5/2$ to $J = 5/2\text{–}3/2$ of the $N = 3\text{–}2$ line and the ratio of $J = 9/2\text{–}7/2$ to $J = 7/2\text{–}5/2$ of the $N = 4\text{–}3$ line are both consistent with the theoretical intensities (Ziurys et al. 1982). The ratio of total integrated intensities $\int T_{MB}(N = 4\text{–}3,\ J = 9/2\text{–}7/2,\ J = 7/2\text{–}5/2)dV/\int T_{MB}(N = 3\text{–}2,\ J = 7/2\text{–}5/2,\ J = 5/2\text{–}3/2)dV$ is 1.40, which is also difficult to explain at 50 K. If the hyperfine sublevels are ignored and a single, common $T_{ex}$ is assumed for all transitions, the ratio of 1.40 corresponds to $T_{ex} = 70$ K [from $T_R(4\text{–}3)/T_R(3\text{–}2) = (4/3)^2 \exp(-h\nu_{43}/kT_{ex})$] in the optically thin limit. These considerations lead us to a most likely possibility that the excitation temperatures are actually higher than 50 K and that the gas temperature is significantly higher than 50 K. In fact, the 800 K cases in our analysis yield density estimates in line with the other molecules. In the present work, therefore, we adopt the 800 K results. The difficulty we met in the 50 K cases is an important indication for a high gas temperature.

One important contributing factor for the high excitation temperature for $C_2H$ compared with other species is its small dipole moment of 0.76 D (see the Appendix). On the one hand, the small dipole moment makes electron collisions less effective even at $x_e = 1 \times 10^{-3}$. On the other hand, $C_2H$ can easily be excited by neutral collisions just like CO. The density estimates with and without electron collisions are, therefore, similar to each other. There remains some uncertainty with regard to neutral collision rates in the present work. As stated in the Appendix, the $C_2H$-neutral collision rates have been estimated from the HCN-He collision rates, since no estimate (theoretical or experimental) is available for $C_2H$-neutral collisions. With this uncertainty in mind, we adopt the result from the 800 K case with electron collisions.

## 4. DISCUSSION

### 4.1. *Characterization of the Emitting Region*

The overall sizes of the emitting regions of $HCO^+$, HCN, and CN are about 13″ including fast and slow velocity components. The emitting regions are clearly smaller than 20″ in diameter, in contrast to the CO (1–0) diameter of ~70″. Based on the similarities in size and spectral shape among the species, we can assume that the molecular lines in the present work (except for CO) originate from the same gas (hereafter referred to as the molecular emission region). The emission lines of the other observed species, $CO^+$, $C_2H$, and $H^{13}CO^+$, probably originate from the same gas as $HCO^+$, HCN, and CN. Since the central 10″ region of NGC 7027 is an H II region, the molecular emission region detected in the present study must be somewhere in a zone with a radial thickness of order 2″ and clearly less than 5″.

While the distribution of emission is reasonably constrained, the distributions of molecules are not necessarily well constrained in the present work. The strong emission from the small central region could couple to the main beam even if the source is outside the half-power beam area.

Even if line emission is detected at 20″–30″ off the center but is weaker than the levels expected from Gaussian coupling as shown in Figures 8–11, then the signal cannot confidently be assigned to the region outside the central emitting region. Since we observed transitions of similar excitation energies, we may also have selectively probed regions of similar physical conditions, density in particular. As noticed by Jaminet et al. (1991), the angular extent of the CO (3–2) emitting region is significantly smaller than the CO (1–0) region, clearly a result of insufficient collisional excitation of CO (3–2) in the outer part of the neutral envelope of NGC 7027. The maximum extent of the $HCO^+$ (1–0) contour is 30″ at detection limit with a synthesized 8″ beam (Likkel 1992). If the beam size is subtracted from the apparent size, the actual size of the $HCO^+$ (1–0) emitting region is about 22″ or less at the detection limit. Thus, $HCO^+$ at a lower density appears to be present to a radius of 11″.

In § 3 we have carried out excitation analyses for four cases of assumed excitation environments. Given that the emitting region is close to the ionized region and that the region is likely subjected to strong UV radiation, the 800 K case with electron collisions appears to be the best approximation to the excitation environment. This case indeed yields the most consistent result in that the estimated $n_{\rm H}$ from six species fall into a narrow range between 1.3 and $5.0 \times 10^5$ cm$^{-3}$, an indication that all the detected emission lines arise from the same gas. The agreement in estimated density between the $HCO^+$ and $H^{13}CO^+$ analyses (despite the intensity difference of factor 40) is an indication of the consistency and reliability of the present analyses.

We did not make analyses separately on different velocity components partly because it would not be reliable in weak lines and partly because a few lines have hyperfine components. Most of the emission in the observed spectra occurs in the central velocity range. For $HCO^+$, for example, about 80% of emission occurs in the central velocity range. The corresponding value for HCN is 70%. Thus, the size and density estimates mostly reflect the slow velocity components.

In search for any hint of peculiar physical conditions in the fast components, we here make a separate analysis on the fast components of $HCO^+$. For the fast blue and red components of $HCO^+$, the line ratio is 1.08 and 1.15, respectively, slightly higher than 0.79 for the total integrated intensities. The corresponding $n_{\rm H}$ is 1.0 and $1.3 \times 10^6$ cm$^{-3}$ for the blue and red fast components, respectively, under the same conditions ($T_k = 800$ K with electron collisions and $N/\Delta V = 2.2 \times 10^{12}$ cm$^{-2}$ km$^{-1}$ s). The density estimates are slightly higher than $\sim 5 \times 10^5$ cm$^{-3}$ for the total emission. The higher density estimates for the fast components, which seem to originate from the inner part of the PDR, could hint to a density gradient through the PDR.

### 4.2. *Chemistry and Comparison with Model*

In the previous subsection we have argued that the excitation environment is best approximated by the case with $T_k = 800$ K and $x_e = 1 \times 10^{-3}$ (with electron collisions). In this subsection we assume that the emitting region (and the best approximation) corresponds to a PDR in NGC 7027 and compare the estimated molecular column densities with model predictions by Hasegawa et al. (2000).

The estimated column densities and molecular abundances are compared with model values by Hasegawa et al. (2000) in Table 3 (Model 1). The estimates from observations are in good agreement with model predictions.

A few failures of the model are (1) the high density ($n_{\rm H} = 8 \times 10^6$ cm$^{-3}$) assumed in the chemical model and (2) the high CS column density (and abundance) predicted in the model. The first problem has become evident in the present work. The present work based on six species constrains the density to $1.3–5 \times 10^5$ cm$^{-3}$ for the central 13″ region in NGC 7027, whereas models with $n_{\rm H} < 1 \times 10^6$ cm$^{-3}$ do not fit observed molecular column densities. Table 3 (Model 2) lists predicted molecular column densities from an unpublished model with $n_{\rm H} = 3.2 \times 10^6$ cm$^{-3}$ by Hasegawa et al. (2000). Models with $n_{\rm H} < 3 \times 10^6$ cm$^{-3}$ yield CN and $C_2H$ column densities significantly below the observed values. The second point was already noted by Hasegawa et al. (2000).

The 3 $\sigma$ upper limit of 0.048 K for $T_{\rm MB}$(CS 5–4) in the present work constrains the abundance and column density of CS to $X({\rm CS}) < 1.3 \times 10^{-9}$ and $N({\rm CS}) < 2.4 \times 10^{13}$ cm$^{-2}$ under physical conditions similar to those for the other molecules in the emission region ($n_{\rm H} = 3 \times 10^5$ cm$^{-3}$, $T_k = 800$ K, and the source size of 13″). Although the upper limit in the present work appears consistent with model predictions, another upper limit by Bachiller et al. (1997) is much lower (see Table 3).

The lack of molecular emission (except for CO) in most of the neutral envelope is consistent with the model. The present observations, however, do not rule out a widespread presence of molecules in the outer part of the neutral envelope. In order to test the model prediction that molecular abundances are very low in the outer part of the neutral envelope (Hasegawa et al. 2000), observations in the lowest rotational lines at a high angular (1″–2″) resolution are necessary.

We started the analysis on the basic premise that all the emission lines arise from a PDR. The estimated densities and molecular abundances are largely consistent with model predictions.

In order to verify the basic assumption, it is necessary (1) to observe molecular lines used in the present study at a 1″ resolution matching the IR $H_2$ imaging observations, and (2) to observe higher excitation lines of the same species to selectively probe the 800 K region at a 10″ or better angular resolution. For example, the lower level of the CO $J = 6–5$ transition lies 83 K above the ground rotational level, so that 50 K gas would not interfere.

### 4.3. $C_2H$

$C_2H$ is an abundant molecule in the CSE of a carbon star (Millar & Herbst 1994; Glassgold 1996). Produced by photodissociation of $C_2H_2$, it attains its peak abundance ($X \sim 10^{-5}$) at $r \sim 0.02$ pc from the central star in its cool phase. In IRC +10216, for example, $N(C_2H) \sim 10^{16}$ cm$^{-2}$. It is possible that the detected $C_2H$ in NGC 7027 is a remnant from the CSE.

In a recent chemical model, however, Hasegawa et al. (2000) propose that most observed molecules including $C_2H$ are newly formed after the remnant molecules from the CSE have been destroyed. Their model predicts $N(C_2H) = 1.5 \times 10^{14}$ cm$^{-2}$ (source averaged) for the hot, dense PDR. The estimate of $2.4 \times 10^{14}$ cm$^{-2}$ for $C_2H$ in § 3.3 is in good agreement with the prediction. The predicted peak abun-

dance of $C_2H$ is $1 \times 10^{-8}$ in the model PDR (Hasegawa et al. 2000). The estimated abundance of $1.1 \times 10^{-8}$ (800 K with electron collisions) is in good agreement with the prediction.

### 4.4. *Origin of the Fast Components*

The observed lines in NGC 7027 commonly show fast components ($V_{LSR} < 10$ km s$^{-1}$, $V_{LSR} > 40$ km s$^{-1}$). At least the fast CO components have very small angular extents. The distributions of the $HCO^+$, CN, and HCN fast components are qualitatively similar to those of the CO fast components. Based on these comparisons, we can assume that all the red and blue fast components in our spectra arise from the same red and blue, respectively, dynamical components near the center. The centers of the fast red and blue components are offset to the south and north, respectively, by about 5″. The geometry of the fast components is not an expanding full sphere.

Recent infrared imaging in the $H_2$ line(s) reveals a geometrically thin ($\sim$1″) $H_2$ emission zone surrounding the central nebulosity of NGC 7027 (Latter et al. 2000; Cox et al. 1997; Hora et al. 1999; Graham et al. 1993; Kastner et al. 1996).

The $H_2$ emission zone is interpreted as an $H_2$ photodissociation zone. The dimension of the $H_2$ PDR shell is about 15″ × 10″. In the latest model by Latter et al. (2000), the PDR shell is approximated by a biconical shell with caps on both openings, where the cap part is moving outward faster than the bulk neutral material.

It is an attractive idea that the fast (and even the slow) components in the molecular spectra presented in this work originate from the geometrically thin $H_2$ emission zone. Models of photodissociation regions predict enhanced molecular abundances in the dissociation front where the abundance of $H_2$ is relatively low (a few percent to 10%; Hasegawa et al. 2000; Yan et al. 1999; Sternberg & Dalgarno 1995). The model by Hasegawa et al. (2000), which has been tailored to NGC 7027, predicts that only such a dissociation zone has significant levels of molecules detected in the present work.

## 5. SUMMARY AND CONCLUSIONS

The profiles of the observed lines in NGC 7027 excluding the CO lines are similar to each other, suggesting a common origin. The regions of bulk $HCO^+$, CN, and HCN emission have similar sizes of order 13″, clearly smaller than 20″ in diameter. These similar characteristics in emission extent and profile among these species suggest that the emission lines originate from the same region. It is a reasonable assumption that the $CO^+$, $H^{13}CO^+$, and $C_2H$ lines also originate from this region. Since the central 10″ region of NGC 7027 is an ionized region, our size estimate leaves $\sim$2″ (clearly less than 5″) for the radial thickness of the molecular emission region.

The observed profiles for the lines of these molecules are very different from those of the CO ($J = 1$–0, 2–1, 3–2) lines, indicating that most of the CO (low-$J$ line) emitting volume does not significantly emit in the $HCO^+$, CN, or HCN line. Our present observations, however, do not rule out a widespread presence of these molecules.

The molecular emission region is very close to the central H II region, so that electrons due to photoionization of carbon are assumed in the excitation analysis. Density estimates from $HCO^+$, $H^{13}CO^+$, $CO^+$, HCN, and CN observations under this assumption fall into a narrow range between 1.3 and $5.0 \times 10^5$ cm$^{-3}$, consistent with the picture that all the observed lines but CO originate from the same gas.

Estimated molecular column densities and relative abundances are in reasonable agreement with model values for a photodissociation region by Hasegawa et al. (2000). The agreement strengthens our suspicions that the observed molecular lines originate from a photodissociation zone and that the molecular abundances are peculiarly high in the photodissociation zone and low elsewhere in the neutral envelope. The isotopomer ratio $HCO^+/H^{13}CO^+$ is 40 in NGC 7027.

Two dynamical components are recognized in the molecular emission region: (1) fast blue and fast red components with velocity shifts more than $\pm$16 km s$^{-1}$ from the systemic velocity, and (2) slow components with velocity shifts within $\pm$16 km s$^{-1}$ from the systemic velocity.

The fast components of $HCO^+$, CN, and HCN have sizes of 7″ $\pm$ 4″. The locations of the blue (red) fast components are offset to the north (south) from the center by several arcseconds, hence a spherically symmetric emitting shell is ruled out. The sizes and offsets are similar to those for the fast components of CO. Therefore, the fast components of $HCO^+$, CN, and HCN probably originate from the same gas as the fast components of CO that have been mapped at high angular resolutions. The assignment of the slow molecular emission to a geometrical or dynamical component is unclear. The estimated size of 13″ for the molecular emitting region applies to the slow velocity components.

From the observed spatial distribution of the molecular emissions and the results of the excitation analysis, we found that the molecular emission region coincides with the recently imaged $H_2$ photodissociation shell observed by the *Hubble Space Telescope*. The derived molecular abundances are also consistent with the predictions of our chemical model, suggesting that photochemistry is actively ongoing in planetary nebulae. While it has long been recognized that planetary nebulae contain remnants of the molecular material ejected during the preceding AGB phase, our work clearly demonstrates that there is a separate, higher temperature, recently formed (within the last $10^3$ yr) molecular shell that is the product of photochemistry. This proposal can be directly tested by imaging observations at a 1″–2″ resolution in individual molecular lines by future submillimeter interferometers.

Since the density and radiation environments of planetary nebulae are well determined from optical/IR/radio observations, and the timescale of chemical reactions is well constrained by the dynamical (expansion) timescale, planetary nebulae therefore represent an excellent laboratory for the study of interstellar chemistry. Further observations with increased sensitivity and resolution, complemented by excitation/chemical analyses similar to those carried out in this work, could provide the necessary constraints to determine the actual chemical network responsible for the production of the rich molecular environment seen in NGC 7027.

We are grateful to H. Matthews and G. Moriarty-Schieven at the Joint Astronomy Centre for obtaining part of the observations for us. The James Clerk Maxwell Tele-

scope is operated by The Joint Astronomy Centre on behalf of the Particle Physics and Astronomy Research Council of the United Kingdom, the Netherlands Organization for Scientific Research, and the National Research Council of Canada. This work is supported by a grant from the Natural Sciences and Engineering Research Council of Canada. S. K. also acknowledges the award of a Killam Fellowship from the Canada Council for the Arts.

## APPENDIX

## ELECTRON AND NEUTRAL COLLISIONS AND MOLECULAR CONSTANTS

For $HCO^+$, the $H_2$-$HCO^+$ de-excitation rates were estimated by multiplying the He-$N_2H^+$ rates in Green (1975) by factors taken from Monteiro (1985). The He-$N_2H^+$ de-excitation rates by Green (1975) were directly used as the He-$HCO^+$ rates. The H-$HCO^+$ de-excitation rates were estimated by multiplying the He-$N_2H^+$ rates by a factor of 2. These de-excitation rates were commonly used in the 50 and 800 K cases because the rates are insensitive to $T_k$. The collisional excitation rates were estimated from the principle of detailed balance and hence were dependent on the gas temperature and the excitation energy. An electric dipole moment of 4.07 D was adopted from Haese & Woods (1979).

Molecular constants were estimated from Lovas (1978, 1992). The collisional de-excitation rates and the dipole moment for $HCO^+$ were used in the excitation calculations of $H^{13}CO^+$. Molecular constants for $H^{13}CO^+$ were estimated from Lovas (1978, 1992). References for dipole moments and molecular constants for $HCO^+$ and other species are summarized in Table 4.

For $CO^+$, the $H_2$-$HCO^+$ rotational de-excitation rates estimated above were used as $H_2$-$CO^+$ rates. Likewise, He-$HCO^+$ de-excitation rates were used as He-$CO^+$ rates. H-$CO^+$ rates were scaled from He-$CO^+$ rates. The collisional de-excitation rates between fine-structure sublevels were estimated by partitioning the pure rotational rates $q(N_u \rightarrow N_l)$ based on the statistical weight $g(J_l)$ of the destination sublevel $(N_l, J_l)$, i.e., by $q(N_u, J_u \rightarrow N_l, J_l) = q(N_u \rightarrow N_l)[g(J_l)/g(N_l)]$. Molecular constants were adopted from Sastry et al. (1981), whereas the dipole moment was taken from Rosmus & Werner (1982) (see Table 4).

For HCN, we adopted the He-HCN collisional de-excitation rates between hyperfine sublevels at 20 K for $0 \leq J \leq 5$ by Monteiro (1984b). For $6 \leq J_u \leq 7$, we used He-HCN de-excitation rates between rotational levels at 100 K by Green & Thaddeus (1974). For $8 \leq J_u$, rates from $J_u = 7$ by Green & Thaddeus (1974) were used. The He rates were then multiplied by factors of 2 and $\sqrt{2}$ to obtain the H-HCN and $H_2$-HCN rates, respectively. The collisional rates between hyperfine sublevels with $6 \leq J_u$ were estimated based on the statistical weight by $q(J_u, F_u \rightarrow J_l, F_l) = q(J_u \rightarrow J_l)[g(F_l)/g(J_l)]$. These collisional de-excitation rates were commonly used in the calculations of the 50 and 800 K cases. References for the adopted dipole moment and molecular constants for HCN are given in Table 4.

For CN, the He-HCN rotational de-excitation rates by Green & Thaddeus (1974) at 100 K were adopted as the He-CN rates. The H-CN and $H_2$-CN collision rates were estimated from the He-CN rates. The rotational de-excitation rates between hyperfine sublevels were estimated by multiplying $g(F_l)/g(N_l)$, i.e., the fractional statistical weight of the destination sublevel. The same set of collisional de-excitation rates were used in the calculations of the 50 and 800 K models. Truong-Bach et al. (1987) used $H_2$-CO rates for $H_2$-CN rates, whereas Bachiller et al. (1997) used $H_2$-CS rates for $H_2$-CN rates. See Table 4 for references for the molecular constants and dipole moment for CN.

For $C_2H$, the He-HCN rotational de-excitation rates (see above) were adopted as the He-$C_2H$ rates. The H-$C_2H$ and $H_2$-$C_2H$ collision rates were scaled from the He-HCN rates. The collision rates between hyperfine sublevels were estimated based on the statistical weight of the destination sublevel. The energy levels were estimated with the analytic expression in Truong-Bach et al. (1987). The relative line strengths of $C_2H$ were adopted from the numerical results in Ziurys et al. (1982) for

TABLE 4

ELECTRON COLLISIONAL DE-EXCITATION RATES AT 50 K

| Molecular Species | $\mu$ (D) | Transition $(u \rightarrow l)$ | $A_{ul}$ ($s^{-1}$) | $q_e(u \rightarrow l)$ ($cm^3\ s^{-1}$) | $\sum q_{H_2}$[a] ($cm^3\ s^{-1}$) | $\sum q_{H_2}/q_e$ (nondim) | $n_{cr}(e)$[b] ($cm^{-3}$) | Reference and Comments |
|---|---|---|---|---|---|---|---|---|
| $HCO^+$ ..... | 4.07 | $J = 4 \rightarrow 3$ | 3.9E−3 | 6.9E−6 | 8.6E−10 | 1.2E−4 | 5.7E2 | 1, 2, 3, 4, 5 |
| $HCS^+$ ..... | 1.86 | $J = 6 \rightarrow 5$ | 3.1E−4 | 1.5E−6 | 3.7E−10 | 2.5E−4 | 2.1E2 | 6, 7, 8 |
| $N_2H^+$ ..... | 3.4 | $J = 4 \rightarrow 3$ | 3.1E−3 | 4.8E−6 | 4.5E−10 | 9.4E−5 | 6.5E2 | 4, 5, 9, 10 |
| $CO^+$ ..... | 2.77 | $N = 3 \rightarrow 2$ | 1.7E−3 | 3.1E−6 | 6.8E−10 | 2.2E−4 | 5.5E2 | 11, 12, $H_2$-$HCO^+$ |
| CO ..... | 0.112 | $J = 3 \rightarrow 2$ | 2.6E−6 | 5.3E−9 | 1.1E−10 | 2.1E−2 | 4.9E2 | 13, 14 |
| CS ..... | 1.958 | $J = 5 \rightarrow 4$ | 3.0E−4 | 1.8E−6 | 1.1E−10 | 6.1E−5 | 1.7E2 | 13, 14 |
| | | $J = 7 \rightarrow 6$ | 8.4E−4 | 1.7E−6 | 1.2E−10 | 6.9E−5 | 4.9E2 | 14 |
| $C_2H$ ..... | 0.76 | $N = 3 \rightarrow 2$ | 5.2E−5 | 2.6E−7 | 9.2E−11 | 3.5E−4 | 2.0E2 | 15, $H_2$-HCN |
| CN ..... | 1.45 | $N = 3 \rightarrow 2$ | 4.1E−4 | 8.9E−7 | 9.2E−11 | 1.0E−4 | 4.6E2 | 15, $H_2$-HCN |
| | | | | | 1.1E−10 | 1.3E−4 | | $H_2$-CO |
| HCN ..... | 2.9846 | $J = 4 \rightarrow 3$ | 2.1E−3 | 3.1E−6 | 1.2E−10 | 3.7E−5 | 6.6E2 | 3, 16 |

[a] Sum of de-excitation rates by $H_2$ collision from an upper rotational level, i.e., $\sum_{l'=0}^{u-1} q_{H_2}(u \rightarrow l')$.

[b] Thermalization electron density: $n_{cr}(e) = A_{ul}/q_e(u \rightarrow l)$.

REFERENCES.—(1) Haese & Woods 1979. (2) Monteiro 1985. (3) Lovas 1978. (4) Lovas 1992. (5) Green 1975. (6) Gudeman et al. 1981. (7) Thaddeus, Guelin, & Linke 1981. (8) Monteiro 1984a. (9) Green, Montgomery, & Thaddeus 1974. (10) Thaddeus & Turner 1975. (11) Rosmus & Werner 1982. (12) Sastry et al. 1981. (13) Lovas & Tiemann 1974. (14) Green & Chapman 1978. (15) Truong-Bach et al. 1987. (16) Green & Thaddeus 1974.

$N \leq 4$ and from the analytic expression in Truong-Bach et al. (1987) for $N \geq 5$. All collisional excitation rates by neutral impact in all our excitation calculations were estimated from the principle of detailed balance.

The rotational excitation of molecules by electron collisions has been incorporated into the excitation analyses of a wide range of interstellar molecules in a series of papers by Turner (1995, 1996 and references therein). We adopt the same assumption as in Turner (1996) that the analytic expressions for electron collision rates by Dickinson et al. (1977) and Dickinson & Flower (1981) can be applied to any dipole permitted rotational transition.

Then, the rate constant for collisional de-excitation by electron impact of a polar molecule is proportional to the line strength of a permitted transition $S_{ul}$, where $u$ and $l$ stand for the upper and lower levels, respectively. The assumption is extended to individual hyperfine transitions in the present work.

The de-excitation rate $q_e^i(u \rightarrow l)$ of a molecular ion by electron collisions is given by

$$q_e^i(u \rightarrow l) = 5.34 \times 10^{-6} T_k^{-1/2} \left(\frac{S_{lu}\mu^2}{g_u}\right)\left[1.21 + E_1(y) + 0.95y\left(1 + \frac{y}{2}\right)^{-3}\right], \tag{A1}$$

$$y = \left(\frac{3.1}{T_k}\right)\left[\frac{1}{2}\left(\frac{h\nu_{ul}}{\mathrm{Ryd}}\right)\right]^{2/3}\left(\frac{\mathrm{Ryd}}{k}\right), \tag{A2}$$

$$E_1(y) = \exp(-y)\ln\left[1 + y^{-1}\exp\left(\frac{-0.577}{1 + 2y}\right)\right], \tag{A3}$$

where $k$ is the Boltzmann constant, Ryd is 1 ryd, $\mu$(debye) is the dipole moment of a target molecule in D, $h\nu_{ul}$ is the energy between levels $u$ and $l$, and $g_u$ is the statistical weight of the starting level $u$ (Turner 1996; Dickinson & Flower 1981). One may have a more intuitive understanding of the nature of the approximation by inserting $S_{lu}\mu^2/g_u = (3hc^3/64\pi^4)(A_{ul}/\nu_{ul}^3)\,\mathrm{D}^{-2}$.

The de-excitation rate $q_e^n(u \rightarrow l)$ of a neutral molecule by electron collisions is given by

$$q_e^n(u \rightarrow l) = 3.56 \times 10^{-6} T_k^{-1/2} \left(\frac{S_{lu}\mu^2}{g_u}\right)[\ln(C\Delta E) + \exp(x)E_1(x)], \tag{A4}$$

where $x = h\nu_{ul}/kT_k$ and $\ln(C\Delta E) = 1.566 - 1.18\mu^{-3} - \ln(\mu)$ for $\mu > 1.53$ D. For $\mu < 1.53$ D, $\ln(C\Delta E) = 0.812$ (Turner 1996; Dickinson et al. 1977).

The excitation rates are estimated from the principle of detailed balance. We ignored electron collisions for dipole forbidden transitions. The electron collision rates for forbidden transitions ($\Delta J \geq 2$) appear to be small at about 1/100 of those for permitted transitions, at least for CN (Allison & Dalgarno 1971).

To illustrate the magnitudes of the electron collision rates, we compare electron and $H_2$ collision rates at 50 K for pure rotational transitions in Table 4, where hyperfine sublevels are ignored. The collision rate from level $u$ to level $l$ by impact of particle $X$ is denoted as $q_X(u \rightarrow l)$ in the table. Since the de-excitation by $H_2$ collisions occurs for any change in rotational quantum number, the sum of $H_2$ rates for collisional de-excitation to all lower levels is given in Table 4. The quantity $\sum q_{H_2}/q_e$ in the table corresponds to the characteristic fractional ionization above which the electron collisions will dominate the collisional process. Also given in the table is the thermalization (or critical) electron density $n_{cr}(e)$ $[= A_{ul}/q_e(u \rightarrow l)]$ for transition $u \rightarrow l$.

From Table 4, it is clear that almost all common molecules except for CO will be affected by electron collisions if the fractional ionization is higher than a few times $10^{-4}$.

## REFERENCES


Aitken, D. K., & Roche, P. F. 1983, MNRAS, 202, 1233
Allison, A. C., & Dalgarno, A. 1971, A&A, 13, 331
Apponi, A. J., Pesch, T. C., & Ziurys, L. M. 1999, 519, L89
Arens, J. F., et al. 1984, ApJ, 279, 685
Bachiller, R., Forveille, T., Huggins, P. J., & Cox, P. 1997, A&A, 324, 1123
Bieging, J. H., Wilner, D., & Thronson, H. A., Jr. 1991, ApJ, 379, 271
Cernicharo, J., Liu, X.-W., Gonzalez-Alfonso, E., Cox, P., Barlow, M. J., Lim, T., & Swinyard, B. M. 1997, ApJ, 483, L65
Cox, P., et al. 1997, A&A, 321, 907
Dayal, A., et al. 1999, BAAS, 31, 1536
Deguchi, S., Izumiura, H., Kaifu, N., Mao, X., Rieu, N.-Q., & Ukita, N. 1990, ApJ, 351, 522
Deguchi, S., Izumiura, H., Rieu, N.-Q., Shibata, K. M., Ukita, N., & Yamamura, I. 1992, ApJ, 392, 597
Dickinson, A. S., & Flower, D. R. 1981, MNRAS, 196, 297
Dickinson, A. S., Phillips, T. G., Goldsmith, P. F., Percival, I. C., & Richards, D. 1977, A&A, 54, 645
Glassgold, A. E. 1996, ARA&A, 34, 241
Goldreich, P., & Kwan, J. 1974, ApJ, 189, 441
Graham, J. R., Serabyn, E., Herbst, T. M., Matthews, K., Neugebauer, G., Soifer, B. T., Wilson, T. D., & Beckwith, S. 1993, AJ, 105, 250
Green, S. 1975, ApJ, 201, 366
Green, S., & Chapman, S. 1978, ApJS, 37, 169
Green, S., Montgomery, J. A., Jr., & Thaddeus, P. 1974, ApJ, 193, L89
Green, S., & Thaddeus, P. 1974, ApJ, 191, 653
Gudeman, C. S., Haese, N. N., Piltch, N. D., & Woods, R. C. 1981, ApJ, 246, L47
Haese, N. B., & Woods, R. C. 1979, Chem. Phys. Lett., 61, 390
Hasegawa, T., Volk, K., & Kwok, S. 2000, ApJ, 532, 994
Hora, J. L., Latter, W. B., & Deutsch, L. K. 1999, ApJS, 124, 195
Jaminet, P. A., Danchi, W. C., Sutton, E. C., Russell, A. P. G., Sandell, G., Bieging, J. H., & Wilner, D. 1991, ApJ, 380, 461
Justanont, K., et al. 2000, A&A, 360, 1117
Kahane, R., Cernicharo, J., Gomez-Gonzalez, J., & Guelin, M. 1992, A&A, 256, 235
Kastner, J. H., Vrtilek, S., & Soker, N. 2001, ApJ, 550, L189
Kastner, J. H., Weintraub, D. A., Gatley, I., Merrill, K. M., & Probst, R. G. 1996, ApJ, 462, 777
Latter, W. B., Dayal, A., Bieging, J. H., Meakin, C., Hora, J. L., Kelly, D. M., & Tielens, A. G. G. M. 2000, ApJ, 539, 783
Latter, W. B., Walker, C. K., & Maloney, P. R. 1993, ApJ, 419, L97
Likkel, L. 1992, ApJ, 397, L115
Liu, X.-W., et al. 1996, A&A, 315, L257
———. 1997, MNRAS, 290, L71
Lovas, F. J. 1978, J. Phys. Chem. Ref. Data, 7, 1445
———. 1992, J. Phys. Chem. Ref. Data, 21, 181
Lovas, F. J., & Tiemann, E. 1974, J. Phys. Chem. Ref. Data, 3, 609
Masson, C. R. 1986, ApJ, 302, L27
Masson, C. R., et al. 1985, ApJ, 292, 464
Middlemass, D. 1990, MNRAS, 244, 294
Millar, T. J., & Herbst, E. 1994, A&A, 288, 561
Monteiro, T. 1984a, MNRAS, 210, 1
———. 1984b, MNRAS, 211, 257
———. 1985, MNRAS, 214, 419

Natta, A., & Hollenbach, D. 1998, A&A, 337, 517
Péquignot, D. 1997, in IAU Symp. 180, Planetary Nebulae, ed. H. J. Habing & H. J. G. L. M. Lamers (Dordrecht: Kluwer), 167
Robberto, M., Clampin, M., Ligori, S., Paresce, F., & Staude, H. J. 1993, A&A, 280, 241
Rosmus, P., & Werner, H.-J. 1982, Mol. Phys., 47, 661
Sastry, K. V. L. N., Helminger, P., Herbst, E., & de Lucia, F. C. 1981, ApJ, 250, L91
Sopka, R. J., Olofsson, H., Johansson, L. E. B., Rieu, N.-Q., & Zuckerman, B. 1989, A&A, 210, 78
Sternberg, A., & Dalgarno, A. 1995, ApJS, 99, 565
Thaddeus, P., Guelin, M., & Linke, R. A. 1981, ApJ, 246, L41
Thaddeus, P., & Turner, B. E. 1975, ApJ, 201, L25
Truong-Bach, Nguyen-Q-Rieu, Omon, A., Olofsson, H., & Johansson, L. E. B. 1987, A&A, 176, 285
Turner, B. E. 1995, ApJ, 449, 635
———. 1996, ApJ, 461, 246
Vallèe, J.-P., Guilloteau, S., Forveille, T., & Omon, A. 1990, A&A, 230, 457
Volk, K., & Kwok, S. 1997, ApJ, 477, 722
Yan, M., Federman, S. R., Dalgarno, A., & Bjorkman, J. E. 1999, ApJ, 515, 640
Ziurys, L., et al. 1982, ApJ, 254, 94